Carbon Nanomaterials for Nanofluidic and Membrane Applications

by

Mike Coleman

A thesis
presented to the University of Waterloo
in fulfillment of the
thesis requirement for the degree of
Master of Science
in
Chemistry (Nanotechnology)

Waterloo, Ontario, Canada, 2014

Author's Declaration

I hereby declare that I am the sole author of this thesis. This is a true copy of the thesis, including any required final revisions, as accepted by my examiners.

I understand that my thesis may be made electronically available to the public.

Abstract

The successful fabrication and characterization of carbon nanomaterials as potential next generation materials for nanofluidic and membrane applications was demonstrated by this work. Ion transport through graphene oxide (GO) membranes of various thicknesses were investigated in order to determine the effect of steric interactions on ion selectivity. The diffusive transport rates of two charge equivalent ruthenium complex ions $Ru(bpy)_3^{2+}$ and $Ru(phen)_3^{2+}$, with a sub-angstrom size difference, were distinguishable through GO membranes and were used as a model to investigate pore and slit-dominant hindered diffusion. Analysis of experimental results suggested that ion transport is mostly facilitated by large pores ($\geq$ 1.75 nm in diameter) in relatively thin GO membranes, while slits formed by GO stacking ($\leq$ 1.42 nm in width) become dominant only in thick membranes.

Furthermore, the interlayer spacing and overall pore structure of GO was engineered in order to optimize ion transport rates and create stimuli-sensitive membranes. This was completed by functionalizing GO with two different polymers; linear poly(ethylene) glycol (PEG-L), and poly (*N*-isopropylacrylamide) (PNIPAm). The addition of both PEG-L and PNIPAm polymers altered the nanofluidic channel geometry, significantly increasing the overall ion flux relative to pristine GO membranes. Analysis of the diffusive transport rates of $Ru(bpy)_3^{2+}$ and $Ru(phen)_3^{2+}$ through PEGylated GO membranes showed that the shorter PEG-L polymers tightened up and closed the larger pores, increasing the flux and selectivity while the longer polymers opened up the overall porous structure, increasing flux but not altering the observed selectivity. Ion permeation was recorded through PNIPAm-functionalized membranes for two different temperatures; T $<$ Lower critical solution temperature (LCST) and T $>$ LCST and observed transport rates were significantly higher than both PEGylated and pristine GO membranes. It was concluded that the grafted PNIPAm in the functionalized GO membranes does not undergo a structural change above the LCST and that enhanced ion transport rates at higher temperatures is the result of increased diffusion coefficients.

The work presented herein expands the versatility of GO membranes for molecular sieving and separation applications. Furthermore, findings could give guidance to the rational design of GO membranes for high-precision ion selectivity and molecular sieving.

Acknowledgements

First and foremost, I would like to express my sincerest gratitude to my supervisor, Dr. Shirley Tang, for the opportunity she have provided me over these past years. With her support, I was able to further my knowledge in the field of nanotechnology through graduate research and I am indebted to her in this regard.

I would also like to thank my committee members Dr. David Cory and Dr. Mikko Karttunen for their assistance and guidance, as well as Mohamad Niknam from Dr. David Cory's research group for his assistance.

Finally, I would like to thank past and present members of Dr. Shirley Tang's research group including Dr. David Donkor, Gaganprit Gill, Dr. Mahyar Mazloumi, Samaneh Shadmehr, Louis Cheung, Xiguang Gao, Zhi Li, Yverick Rangom, Kai Wang, Andrew Ward, and Yun Wu.

Table of Contents

List of Tables

List of Figures

List of Abbreviations

AAO: Anodized Aluminum Oxide

AFM: Atomic Force Microscopy

ATP: Adenosine triphosphate

bpy: 2,2'-bipyridine

DI: Deionized

DMSO: Dimethyl sulfoxide

CNT: Carbon Nanotube

CVD: Chemical Vapour Deposition

DLS: Dynamic Light Scattering

DMSO: Dimethyl Sulfoxide

DNA: Deoxyribonucleic acid

EDC: 1-Ethyl-3-(3-dimethylaminopropyl) carbodiimide

EDL: Electric Double Layer

FTIR: Fourier Transform Infrared Spectroscopy

GLUT1: Glucose Transporter

GO: Graphene Oxide

LCST: Lower Critical Solution Temperature

MD: Molecular Dynamics

MES: 2-(N-morpholino)ethanesulfonic acid

MLCT: Metal to Ligand Charge Transfer

NHS: N-Hydroxysuccinimide

NMR: Nuclear Magnetic Resonance

PC: Polycarbonate

PDMS: Polydimethylsiloxane

PEG-L: Linear poly(ethylene) glycol

phen: 1,10-phenanthroline

PMF: Potentials of Mean Force

PNIPAm: Poly(*N*-isopropylacrylamide)

PNP: Poisson-Nernst-Plank

PS: Polystyrene

SEM: Scanning Electron Microscopy

XRD: X-ray Diffraction

Chapter 1

Introduction

Membranes are materials that restrict the flow of ions or molecules in transport media[1] and are widely used in food processing,[2,3] bioreactors and biotechnology,[4] natural gas purification,[5] fuel cells[6] and water purification.[7–11] Due to the vast applications, specific performance requirements may vary; however, improving general metrics such as high analyte recovery (or retention), high analyte selectivity, low fouling, low energy consumption, low fabrication and operating costs are performance characteristics that drive the advancement of membrane materials. In addition, improving a membrane's ability to withstand thermal, mechanical and/or chemical degradation are also acceptable performance characteristics.

There have been many different approaches towards improving membrane performance. The biomimetic approach, which aims to fabricate synthetic nanoporous materials and membranes that mimic biomolecules such as aquaporin-1, P-type ATPase Na^+/K^+ ionic pumps or glucose transporter (GLUT1) molecular trafficking platforms found in biological cells, is popular for designing membranes for molecular sieving, sensing, and drug delivery applications due to the highly selective capabilities, efficiency and transport rates of these biological systems.[10,12]

Carbon nanomaterials such as carbon nanotubes (CNTs) along with graphene and its chemical derivatives such as graphene oxide (GO) are expected to show great promise as synthetic nanoporous materials due to their increased hydrodynamic, gaseous and electrokinetic transport compared to conventional systems. CNTs can be fabricated into high density, alignable arrays with uniform pore distributions, while graphene and its derivatives (such as GO) can be fabricated with tunable thicknesses, surface areas and functionalities; all favourable traits of a membrane platform.

1.1 Mass Transport Phenomena

There are many forces that can cause the flux of ions or molecules through a membrane separating two media; chemical potential $\Delta\mu$, pressure ΔP, temperature ΔT and/or electrical potential $\Delta\Psi$.[1] Although all of these can have significant influence on the operation of membranes, the focus in this chapter will be towards utilizing differences in chemical potential (concentration-driven diffusion) and electrical potential (electro-osmosis and electrophoresis) to drive ions and molecules through carbon nanomaterial-based systems.

1.1.1 Diffusion

Concentration-driven diffusion is the net movement of a solute from a domain of high chemical potential to a domain of low chemical potential without the assistance of external stimuli such as convection or advection. The flux of molecule or ion i along the x direction is given by,

$$J_i = \frac{D_i}{RT} C_i \left(-\frac{d\mu_i}{dx} \right) \tag{1.1}$$

$$J_i = -D_i C_i \left(\frac{d \ln a_i}{dx} \right) \tag{1.2}$$

where D_i is the diffusion coefficient, R is the gas constant, T is the temperature, μ is the chemical potential, C_i is the concentration, and a_i is the activity of the ion or molecule in solution. Substituting $a_i = C_i \gamma_i$ where γ_i is the activity coefficient (and assuming the ideal case where γ_i is constant), one obtains[1]

$$J = -D_i \frac{dC_i}{dx} \tag{1.3}$$

which is Fick's First Law of diffusion.

At the nanoscale, hindered diffusion is important for transport in pores of molecular dimensions because the pore dimensions are of the same order as those of a solute molecule.[13]

Hindered diffusion takes into account the increased drag on a sphere translating parallel to the pore axis and the velocity of a freely suspended sphere to lag behind the approach velocity of the fluid.[13,14] At this scale, any steric restrictions or long-range intermolecular forces will affect the radial distribution of the solutes, which results in modifications to the overall hydrodynamic behaviour within the pores.

The diffusion equation including the effects of steric hindrance,

$$J = -H(\lambda) D_i \frac{dC_i}{dx} \tag{1.4}$$

gives the flux of an uncharged solute along the x-axis in terms of the diffusion coefficient and the concentration gradient driving the diffusion. The overall hindrance coefficient $H(\lambda)$ in Equation 1.4 takes into account the diffusive hindrance $K_d(\lambda)$ and the equilibrium partition coefficient $\Phi(\lambda)$, which represents the ratio of the average concentration in the pore to the bulk concentration.[13,14] The overall diffusive hindrance coefficient $H(\lambda)$ is written as,

$$H(\lambda) = \Phi(\lambda) K_d(\lambda) \tag{1.5}$$

For purely steric interactions, the hard-shell approximation for $\Phi(\lambda)$ which assumes solutes as small spheres is provided below,

$$\Phi = \begin{array}{ll} (1-\lambda)^2 & \text{for cylindrical pores} \\ (1-\lambda) & \text{for slit pores} \end{array} \tag{1.6}$$

where λ represents the relative solute size (dimensionless) calculated as the radius of the solute a divided by the radius or half-width of the pore h, as shown in Figure 1.1. Small values for $\Phi(\lambda)$ indicate that the solute concentration inside the pore compared to the bulk concentration is low, while high values towards unity indicate that the average concentration inside the pore is higher compared to bulk. In addition to geometry, the equilibrium partition coefficient $\Phi(\lambda)$ has been shown to be a function electrostatic interactions between the solute and the pore wall.[15–17] It has been seen that the partition coefficient decreases away from the hard-shell approximation of Equation 1.6 with decreasing ionic strength

(defined by the dimensionless parameter κa where κ is the Debye-Hückel parameter and a is the solute radius) for repulsive electrostatic interactions whereas it increases towards the hard-shell approximation of Equation 1.6 (or even greater than one) for attractive interactions.[15–17]

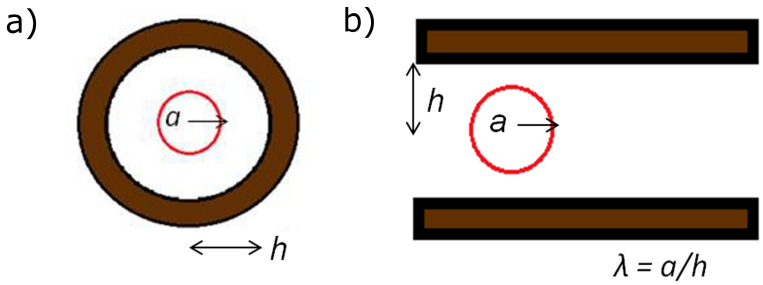

Figure 1.1: Schematic drawings of the pores in membrane modelled as either (a) cylindrical pores or (b) slits. The ion radius, pore half width, and relative ion size are denoted as a,h, and $\lambda = a/h$, respectively.

Theoretical expressions of K_d in Equation 1.5 has been extensively developed in order to predict the effect of size, shape, and electrical charge of the solutes and pores on the diffusive transport characteristics of membranes.[13,14] Variations in these expressions depend on desired accuracy, approximations used to model the system, and the range of λ which the equation is valid. For example, the commonly used Renkin equation uses the centreline approximation and is only valid for $\lambda < 0.4$.[13] Meanwhile, the Bungay & Brenner equation, which also uses a centreline approximation, is valid for all values of λ.[13,18] To elaborate on the importance of modeling approximations, there are caveats to note when using centreline approximations to evaluate K_d; first, the centreline approximation models small, neutral spherical solutes and the calculations assume that long-range interactions between the solute and the pore wall are negligible. If solute-wall interactions are repulsive, solutes will prefer centreline positions due to symmetry, resulting in increased accuracy from these equations. However, for attractive solute-wall interactions, the centreline approximation loses accuracy as the solutes migrate off-axis. Second, results using centreline approximations will be slightly higher than off-axis approximations, as solutes experience lesser drag farther from the pore wall, increasing the hindrance coefficient towards unity. As a result, it is important to utilize the expression for K_d that best matches the system under

investigation.

1.1.2 Electrokinetics

Expanding on Equation 1.3, the flux of molecule or ion i along the x direction due to an electrical potential differential $\Delta\Psi$ is given by,

$$J_i = -u_i z_i C_i \left(\frac{d\Psi_i}{dx}\right) \tag{1.7}$$

where u_i is the mobility of the molecule or ion in the solvent media, and z_i is the valency of the ion. Substituting $u_i = D_i F/RT$ where F is Faraday's constant, one obtains

$$J_i = -D_i \left(\frac{z_i F}{RT}\right) C_i \left(\frac{d\Psi_i}{dx}\right) \tag{1.8}$$

Therefore, by combining Equations 1.3 and 1.8, and including the effects of convection (for the sake of completion), the total flux of a molecule or ion i along the x direction in an ideal system is given by the Nernst-Plank Equation[1,19]

$$J_i = -D_i \frac{dC_i}{dx} - \frac{z_i F}{RT} D_i C_i \frac{d\Psi_i}{dx} \pm v_c C_i \tag{1.9}$$

where J_i, D_i, C_i, F, R, z_i, dC_i/dx, and $d\Psi/dx$ have been defined earlier and v_c is the convective velocity field. The first term of Equation 1.9 is from diffusional contributions, the second from electromigration, and the third from convective transport.

Electro-osmosis is the movement of the solution ions neighbouring a surface in the electric double layer (EDL) as a result of an applied electric field.[19] The electro-osmotic velocity of these ions can be calculated using Equation 1.10,

$$\nu_{eo} = \frac{-\epsilon_0 \epsilon_r E_i \zeta}{\eta} \tag{1.10}$$

where ϵ_0 is the permittivity of free space, ϵ_r is the dielectric constant of the solution medium, E_i is the electric field in the i direction, η is the dynamic viscosity and ζ is the zeta-potential.

In addition, the electro-osmotic mobility can be defined by,

$$\mu_{eo} = \frac{-\epsilon_0 \epsilon_r \zeta}{\eta} \tag{1.11}$$

where the variables are the same as those in Equation 1.10.

Electrophoresis, on the other hand, is the movement of the solute ions in the opposite direction of the solution molecules as a result of an external electric field.[19] Electrophoretic mobility is ultimately dependent on the EDL, thus it can have two different values depending on the thickness of the double layer. If the EDL is thin, such that the solute particle radius is greater than the thickness of the EDL (or $\kappa a \gg 1$ where κ is the Debye-Hückel parameter and a is the solute particle radius,) the electrophoretic mobility can be written as Equation 1.11. If the thickness of the EDL is greater than the solute radius ($\kappa a \ll 1$) the electrophoretic mobility approaches the Hückel-Onsager limit,[19]

$$\mu_{ep} = \frac{-2\epsilon_0 \epsilon_r \zeta}{3\eta} \tag{1.12}$$

and as a result, the electrophoretic velocity can be written as,

$$\nu_{ep} = \mu_{ep} E_i \tag{1.13}$$

In the following sections, the use of concentration-driven diffusion, electro-osmosis and electrophoresis to control ion transport through carbon nanotubes and graphene-based membranes and devices will be explored.

1.2 Ion Transport in Carbon Nanotubes for Membrane Applications

Initial developments using carbon nanotubes as the main component for membranes and nanofluidic devices came from Hummer *et al.* who investigated the spontaneous and continuous filling of carbon nanotubes with water molecules.[20] They simulated the molecular behaviour of water in a 13.4 Å long, 8.1Å diameter single-walled carbon nanotube over 66 ns and found that the water molecules found inside the nanotube re-configured their bulk tetrahedral hydrogen-bond network to form a one-dimensional hydrogen-bonded chain. Formation of the chain configuration partially compensated for the energy cost resulting from the water molecules losing two of the four hydrogen bonds, and they found that the water chain had no interactions with the hydrophobic nanotube wall that would result in scattering or rotation of the water molecules and destabilize the hydrogen bond ordering. This resulted in pulsating water transport through the nanotube with velocities on the same magnitude as water transport through transmembrane proteins and orders of magnitude faster than other synthetic nanoporous systems.

Additional molecular dynamics (MD) simulations of water transport through carbon nanotubes confirmed these initial conclusions, attributing the increased water flow velocities to the atomic smoothness of the graphitic surface displaying near-perfect slip properties.[21,22] Joseph *et al.* conducted MD studies that compared the flow rates and velocity profiles of water through both atomically smooth and rough CNTs.[23] When comparing experimental mass flow rates with those rates theoretically calculated from continuum theory, it was found that CNTs with atomically smooth surfaces had an enhancement factor of 2052 while CNTs with atomically rough surfaces only had an enhancement factor of 4.7.

Majumder *et al.* investigated the diffusive mass transport of cations, anions, and neutral organic dye molecules through a carboxyl-functionalized multi-walled CNT membrane with inner diameters of approximately 7 nm.[24] To make the CNT membrane, the authors grew vertically-aligned multi-walled CNTs via chemical vapour deposition (CVD) on a iron catalyst-supported quartz substrate using a ferrocene-xylene-argon-hydrogen gas combination at 700 °C.[25] After growth, the authors spin-coated a 50% w/w polystyrene:toluene

solution and dried the membrane in vacuum for 4 days at 70 °C. To open and functionalize the CNTs with carboxyl groups, the membrane was subjected to a H_2O plasma-enhanced oxidation process at 600 mTorr for 7 minutes. A general CNT membrane setup is shown in Figure 1.2.

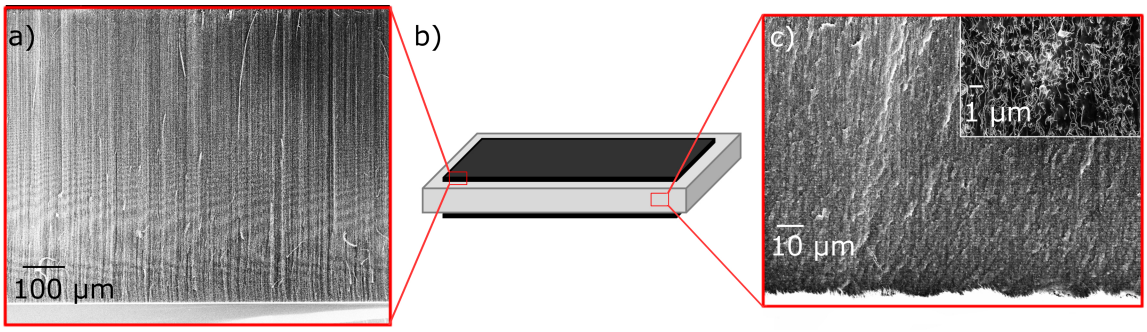

Figure 1.2: Carbon nanotube membrane setup. (a) Cross-sectional scanning electron microscopy image of vertically aligned multi-walled carbon nanotubes. (b) Schematic of carbon nanotubes embedded in a polymer matrix. (c) Cross-sectional scanning electron microscopy image of polydimethylsiloxane coating CNTs. Inset: CNTs embedded in polydimethylsiloxane.

Using the Renkin equation (Equation 1.14) to evaluate K_d and the Stokes-Einstein equation (Equation 1.15) to determine bulk diffusivity values,

$$H(\lambda) = (1-\lambda)^2(1 - 2.104\lambda + 2.09\lambda^3 - 0.95\lambda^5) \tag{1.14}$$

$$D_0 = \frac{k_B T}{6\pi\eta R_s} \tag{1.15}$$

where D_0 is the bulk diffusivity, k_B is the Boltzmann constant, η is the viscosity of the liquid, and R_s is the hydrodynamic radius of the solute molecule, Majumder *et al.* observed that the experimental diffusivity of the various solutes were between the bulk and calculated hindered diffusivity values. They noted that the cationic solutes had diffusivities closer to bulk values as a result of the electrostatic attraction with the anionic carboxyl-functionalized pore entrance, while the anionic and neutral solutes were slower than bulk

and closer to the hindered diffusivity calculations. As a result, the authors concluded that there is minimal if not any enhancement of ion diffusion through CNTs, which has been confirmed by other experiments.[26,27]

Using electro-osmosis, Wu *et al.* examined the electro-osmotic flow properties of CNT membranes with a variety of different inner diameters.[28] Their primary goal was to determine if CNTs will yield highly efficient electro-osmotic flow due to the CNT's atomically flat graphitic planes that allow fast fluid flow.[29,30] This was performed by measuring the fluxes of both charged tris(2,2-bipyridyl) dichlororuthenium(II) $Ru(bpy)_3^{2+}$ molecules and neutral 1,3,7-trimethylxanthine (caffeine) molecules influenced by an external electric field. Under an applied bias ranging from -300 to +300 mV, fluxes of both the $Ru(bpy)_3^{2+}$ and caffeine molecules were studied and observations found that these fluxes were increased under negative bias but decreased under positive bias as expected. The overall flux of the $Ru(bpy)_3^{2+}$ was calculated using Equation 1.9, while the neutral caffeine molecules used a simplified version of Equation 1.9 due its non-dependence on the electric potential as a result of its neutrality. At -300 mV, the maximum electrokinetic values occurred at where the flux of caffeine was valued at 18.2 nmol/hr cm^2, an enhancement factor of 2.7 compared to results obtained at zero bias. The electro-osmotic velocity at 300 mV was calculated to be 0.12 cm $V^{-1}s^{-1}$.

To evaluate the efficiency of the CNT membrane in comparison other platforms, the electro-osmotic flow in the CNT membrane was compared to other nanoporous membranes, mainly anodized aluminum oxide (AAO) membranes, template-prepared CNTs,[31] and AAO membranes with an SO_3^- anion functionalization. The efficiency was defined as the current multiplied by the voltage drop divided by the number of moles transported in a given time interval. Based on the their results, Wu *et al.* saw an enhancement of 25-40 in electro-osmotic efficiency for CNT membranes compared to the other platforms investigated due to CNT's atomically flat graphitic planes allowing fast fluid transport. Wu *et al.* stressed the importance of the increased efficiency because of the potential applications of CNT membranes for chemical sieving and compact medical nanofluidic devices.

Using a CNT membrane setup similar to Figure 1.2, Lee *et al.* developed a two-state

Coulter counter as a result of oscillating electro-osmotic H^+ and OH^- ion currents due to stochastic pore blocking of small cations (Na^+, K^+, and Li^+) in a single, isolated single-walled carbon nanotube.[32,33] Fabricating a CNT membrane by embedding CNTs in an epoxy, the electro-osmotic current of aqueous ionic solutions was monitored. At an optimal voltage determined by the sample, a two-state Coulter counter was obtained as a result of a single ion transport through a single CNT. If a cation entered the pore, the change of the conductance as a result of pore blockage was estimated by relating the ratio of hydration ion diameter to pore diameter, and results showed that an increase in ion hydration diameter resulted in increased conductance changes when pore blocking events occurred.

According to the authors, the oscillating electro-osmotic currents can be physically explained by the coupling of stochastic pore blocking and a proton-diffusion limitation at the pore entrance. The mobility of protons through the CNT calculated by the authors was greater than the mobility in bulk solution. As a result, any proton flux through the carbon nanotube will ultimately deplete the proton concentration at the pore entrance. When this occurs, the local ion concentration increases at the pore entrance, increasing the likelihood of transporting through the carbon nanotube. Once the nanotube is blocked by the ionic species, the proton concentration at the pore mouth replenishes while the blocking cation travels through the nanotube. When the cation exits at the other end, the proton current is restored, and any blocking events are interrupted by the high concentration of protons relative to cations, and the process repeats. To investigate this phenomenon, the authors constructed a stochastic simulation of the system with six equations and their associated rate constants. The noise-defining parameter of the system k_s, which was defined as the rate constant of H^+ diffusion near the pore entrance, was varied to maximize the coherent signal and permit the system to oscillate as explained above. The value of this constant to produce coherence resonance was found to be approximately 7.5×10^3 s^{-1}, which resulted in an ion flux of 480 ions per minute. Using the stochastic resonance phenomena observed in the CNT nanopore, one can extrapolate the methodology to develop a biomolecule sensing platform, as the amplitude of current change, the number of events per unit time, and the dwell time all represent characteristic information used to identify analytes (size, chemical moieties, and concentration, respectfully).[34–36]

Employing electrophoresis, Wu *et al.* investigated the electrophoretic mobility and velocity of ions in single-walled carbon nanotube membranes by actively measuring the ion concentration using inductively coupled plasma atomic emission spectroscopy.[37] Initially, the cationic electrophoretic mobilities of K^+, Na^+, Li^+, H^+, and $Ru(bpy)_3^{2+}$ were measured by applying an external bias across the membrane, and the measurements showed an enhancement of 3 for the electrophoretic transport rates compared to their bulk values. The authors also report the dependence of concentration on the electrophoretic mobilities of K^+ and noted higher electrophoretic K^+ mobility for lower ion concentrations (1-6 mM) than those observed for higher concentrations (40 mM) as a result of higher electro-osmotic velocity. At low concentrations, the Debye screening length (approximately 9.6 nm at 1 mM) is larger than the diameter of the CNT (0.9 nm), thus anions at the pore entrances are rejected and cationic transport is enhanced. At higher concentrations, the Debye screening length is reduced to that of the diameter of the CNT, thus anions at the pore entrances are no longer screened and cationic transport is hindered by the resulting electro-osmotic velocity of the solution in the opposite direction. The ionic flux of K^+ and the resulting ionic current through the CNT membranes was measured to confirm the ionic current and flux obtained from electrophoretic mobility calculations, and their results from both experiments were within 30 percent of each other.

Using electrophoretic transport, an ionic size-exclusion rectifying diode device was demonstrated.[37] Initially, one side of the membrane was filled with $Fe(CN)_6^{3-}$ and the other side was filled with $Ru(bpy)_3^{2+}$. When a negative bias was applied to the working electrode, the $Fe(CN)_6^{3-}$ and $Ru(bpy)_3^{2+}$ were forced through the CNT. Since the total diameter of these two ions are greater than the diameter of the nanotube, the ions were confined within the nanotube and pore blockage occurred, cancelling out any current. When positive bias was applied, the smaller counter-ions (K^+ and Cl^-) were capable of transport across the membrane, thus inducing an ionic current. When the working and reference electrodes were reversed and the bias was applied, opposite rectifying currents were recorded.

Similarly, an ionic surface charge exclusion rectifying diode was developed by Scruggs *et al.* that utilized an asymmetric poly-(dimethylamine-*co*-epichlorohydrin) polycation pore entrance functionalization on a CNT membrane.[38] Scruggs *et al.* analyzed the rectification

ratio, R, which is defined as the reverse-bias current divided by the forward-bias current as a function of salt concentration and applied bias. Varying both the salt concentration and applied bias, their experiments resulted in a maximum rectification ratio of approximately 6 at 10 mM concentration and 450 mV applied bias. At concentrations higher than 10 mM, the rectification ratio reduced to a value of 3 as a result of the reduced Debye screening length no longer effectively screening the anions at the pore entrance. To verify their findings, they theoretically calculated the ionic flux using a one-dimensional solution to the Poisson-Nernst-Plank (PNP) equation.[39] The PNP equation combines Equation 1.9 without the convective transport term and the Poisson equation,

$$\epsilon_0 \epsilon_r \nabla^2 \Phi = e(C_+ - C_-) \tag{1.16}$$

where ϵ_0 is the permittivity of free space, ϵ_r is the dielectric constant of the solution medium, e is the elementary charge, $C_\pm$ are the concentrations of the cations and anions respectfully, and Φ is the electric potential. The theoretical PNP model used in this endeavour provided a qualitative explanation to the rectification of ionic current as a result of polycation modification; however, it provided a poor match to experimental results at salt concentrations other than 10 mM; however, the model was inaccurate at explaining overall results since the authors had to alter the surface charge density values for each salt concentration, and did not include electro-osmotic flow through the nanotube during the development of the model.

1.3 Ion Transport in Graphene and Graphene Oxide for Membrane Applications

Coincidentally to CNTs, early developments in graphene-based membranes focused on the simulations of water and ions through graphene nanopores; a single planar graphene sheet with a pore of a specific radius constructed by removing the carbon atoms from the graphene sheet.[40–44]

Sint *et al.* used MD simulations to investigate the ion selectivity of F-N and H-functionalized

graphene nanopores.[41] In each simulation, the negatively charged F-N-nanopore favoured the passage of Na^+, Li^+, and K^+ while the positively charged H-nanopore only passed the Cl^- and Br^-. They attributed the selectivity of the nanopore to the electrostatic interactions between the functionalized moieties and the ions. They also found that the smaller ions had lower passage rates through the nanopore, mainly due to the dehydration requirement of the solvated ion. Similar results were found by Cohen-Tanugi *et al.* who simulated the desalination dynamics of a graphene nanopore in NaCl electrolyte under varying applied pressures.[45] By varying the pore diameter and the pore chemistry, the authors found that the pores must not exceed 5 Å in diameter in order to effectively hinder ions from passing through the membrane. Furthermore, they found that the hydrogenated pores limit the ion transport through the pore more than hydroxylated pores. This is mainly due to the hydroxylated pores lowering the free energy barrier, facilitating transport of ions through the membrane.

Experimentally, diffusion through intrinsic nanopores in single layer CVD graphene was investigated by O'Hern *et al.* who grew single layer graphene on copper via CVD and transferred it onto a porous polycarbonate track etch membrane.[44] Using scanning transmission electron microscopy, it was found that the CVD graphene had intrinsic 1-15 nm pore defects in a pattern that mimicked the surface topography of the copper. Although the source of the defects is currently unknown, these pores exhibited ion selectivity to KCl, Allura Red AC, tetramethylammonium chloride, and tetramethylrhodamine dexran due to steric hindrance when subjected to both pressure-driven and diffusive transport. To follow up these initial experiments, O'Hern *et al.* fabricated sub-nanometer pores with tunable diameters, high uniformity and high areal density over macroscopic areas of single layer graphene.[46] The authors nucleated reactive defects on the graphene sheet through ion bombardment and then subjected the sheets to oxidative etching to grow them into pores. Prior to etching, baseline measurements in KCl, and Allura Red AC transport, as well as membrane potential, were monitored and transport was comparable to previous measurements associated with transport through defects and micrometer-sized tears in the graphene.[44]

At certain time intervals during the etching process, KCl and Allura Red AC transport,

as well as membrane potential, were monitored in order to reveal the effect of pore size on selectivity and etch time. At an etch time of 5 minutes, the membrane potential and KCl diffusion increased, indicating partial selectivity to K over Cl^- due to the negative functional groups terminating the edge of the pore, similar to Sint *et al.* who observed selective cation and anion transport based on pore functionalization.[41] As the etch rate increased, the selectivity between K^+ and Cl^- ions diminished and eventually plateaued after 25 minutes of etching. Meanwhile, Allura Red AC remained unchanged until the etching process reached 60 minutes, illustrating steric pore blocking for the larger Allura Red molecule until this time. Finally, at 120 minutes, the transport of KCl and Allura Red were identical to the polycarbonate support membrane. These results demonstrated that single layer graphene membranes consisting of nanopores can exhibit tunable steric selectivity and transport by controlling the etch time.

Since a majority of graphene-based membranes will comprise of more than a single layer of graphene, it is more practical to investigate water and ion transport through graphene oxide (GO), the two-dimensional amphiphilic and solution-processable chemical derivative of graphene that consists of crystalline graphitic domains, highly disordered oxygenated regions, and nanosized pores.[47–49]

GO membranes can be synthesized by layer-by-layer assembly,[50] drop-casting,[51] or vacuum filtration.[52–55] All of these methods use aqueous GO solution which makes fabrication easy; however, the major concern regarding their use in aqueous media is GO's ability to re-disperse in water due to the strong hydrophilic character of the nanosheets. To overcome this drawback, one can either use additional membranes such as polycarbonate or anodized aluminum oxide as support layers, or one can functionalize the GO nanosheets and cross-link individual layers either covalently or non-covalently.[56]

Since GO has both crystalline graphitic domains and oxygen-based functional groups, vast chemical options are available in order to control the charge, functionality, and interlayer spacing of GO. For example, one could covalently attach amine-terminated molecules by converting the carboxylic acid groups into amide groups using carbodiimide chemistry,[57] or one could attach molecules onto the graphitic regions by using diazonium salts.[56] From

a non-covalent perspective, one can functionalize GO using ligands via $\pi - \pi$, cation-π, or anion-π interactions. The schematic of GO, membrane formation, and possible functionalization, is shown in Figure 1.3.

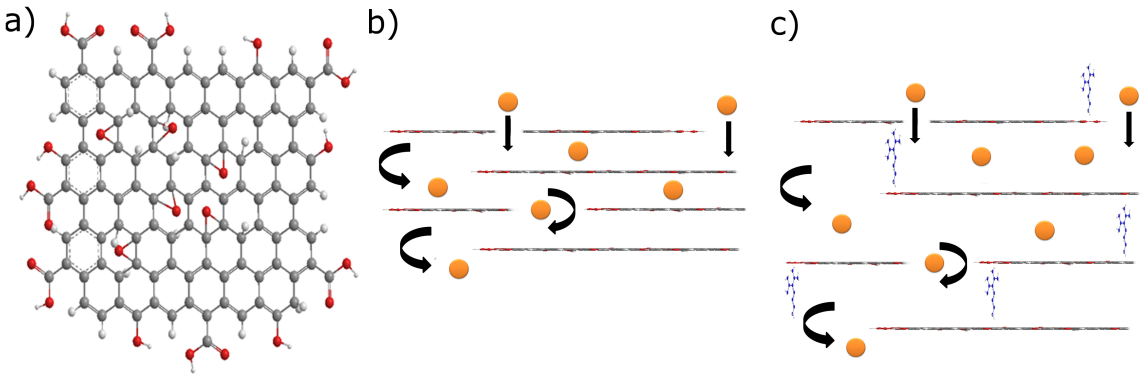

Figure 1.3: (a) Schematic drawing of GO sheet. Red, white and grey atoms correspond to oxygen, hydrogen and carbon atoms, respectfully. (b) Ion or small molecule transport through GO membrane consisting of stacked GO sheets. (c) Effect of functionalization on GO membrane.

Experiments have found that there is no impedance on water permeation through GO membranes or correlation between the hydrodynamic flux and the number of GO layers, citing transport similarities to carbon nanotubes.[50,58,59] Furthermore, Boukhvalov *et al.* investigated the origin of anomalous water permeation through GO membranes and noted a highly symmetric hexagonal ice monolayer over the pristine sp^2 network of GO can slide isotropically as a whole across the graphitic surface.[60] However, the migration along the zigzag direction of the graphitic surface is most energetically favourable due the large distances between hydrogen atoms facilitating easy hydrogen bond breaking between ice layers. At the edge of the sheet, in the case of an ice monolayer, it is more energetically favourable for the monolayer to continue to slide along the nanocapillary network than to pass through the void in the GO sheet. However, in the case of a bilayer, the presence of hydroxyl functional groups stimulates the destruction of one of ice layers comprising the bilayer, followed by the water molecules then penetrating through to the subsequent interlayer spacing, forming another ice bilayer. Finally, trilayer energetics were investigated and found to be similar to monolayers, thus highlighting the unique dependence of the

interlayer spacing on water transport.

Similarly, Wei *et al.* investigated water transport in GO using molecular simulations, and found that the slip length, contract angle, and flow enhancement between water and GO have a strong dependence on the interlayer spacing and concentration of hydroxyl groups along the basal planes.[61–63] The slip length, defined as the extrapolated distance relative to the wall surface where the velocity is equal to zero, decreased from 48±4.02 nm to 0.44± 0.12 nm as the concentration of hydroxyl group increased to 30%, mainly due to the presence of any hydroxyl groups disrupting the pristine graphene surface. In addition, Wei *et al.* performed molecular dynamics simulations to explore the wetting properties of GO.[61,62] By varying the concentration of oxygen-containing functional groups, oxidation pattern, and sheet corrugation, the authors noted the contract angle between water and the GO surface decreased as the concentration of hydroxyl groups increased, altering the hydrophobicity of the GO. Furthermore, as the distance between two adjacent oxygen-containing functional groups increased, the authors noticed lower contact angles while sheets whose corrugation amplitude was large and/or wavelength was short resulted in higher contact angles. For flow enhancement and velocity profiles, at interlayer distances less than 0.7 nm, water forms a monolayer with hydrogen bonds forming with the hydroxyl groups; bilayer and trilayers of water exist at interlayer distances of 1.0 and 1.4 nm, respectively, consistent with other work.[52] The velocity profiles of water at these distances approach parabolic flow profiles as the interlayer distance increases and/or at high hydroxyl concentrations, implying the possibility of using continuum hydrodynamic theories to analyze and model the transport through GO. However, it was reported that although the water-graphene interface features low friction due to the atomically smooth graphitic surface (and thus experiences enhanced hydrodynamic flow), water transport between oxidized regions around the pristine nanochannels reduces the expected flow enhancement as a result of the hydrogen bonding between the water molecules and the oxygen-containing functional groups.[63] In addition, it was found that the flow enhancement decreases as the interlayer spacing increases, and the voids between adjacent GO sheets produce water transport similar to bulk with no significant enhancement. These conclusions suggest that the reported fast hydrodynamic flow through graphene-based membranes is due to their porous microstructures more so than the slip at the water - graphene interface.

Raidongia *et al.* investigated the ion permeation characteristics of GO membranes at equilibrium with various electrolyte solutions, and noticed that at high salt concentrations, the ionic transport through the GO nanochannels behaves similar to bulk.[53] At low salt concentrations, higher-than-bulk cationic transport occurred due to electrostatic attraction from the negatively charged functional groups. The authors acclaim the benefits of using GO for nanofluidic devices for multiple reasons, mainly the scaling capabilities and ease to fabricate and modify. The individual two-dimensional graphene oxide nanosheets, which are stacked via filtration, form membranes whose thickness and lateral dimensions can easily be adjusted based on the amount of GO solution and filtration setup. Secondly, the surface charge, interlayer thickness, and ion selectivity can be all modified by chemically functionalizing the graphene oxide.

This observation extends to partially-reduced GO, where the negatively charged nanochannels stilled displayed surface-charge-governed ion transportation at a C/O ratio of 10:1 (compared to conventional GO membranes which have C/O ratios of 2-3:1).[64] These partially-reduced GO membranes, whose thickness ranged between 5-200 microns, preferentially permeated counter-ions and excluded co-ions when a gas pressure differential was applied across the membrane. These pressure differentials, when between 2-8 kPa, resulted in linearly dependent ionic currents as a result of the continuous hydraulic flow. This identified the partially-reduced GO membrane capable of ion selectivity as well as hydraulic-electric conversion.

Furthermore, Sun *et al.* fabricated GO membranes ($\leq$10 μm) via drop-cast method and the authors found that ion selectivity was associated to the interaction strength between the metal ions and the GO membrane, as decreasing permeability did not correlate to increasing hydrated radii size.[51] The authors noticed the diffusive permeation of heavy metal salts were significantly lower than ionic salts due to the tight coordination between the heavy-metal ion and the GO functional groups. In addition, strong acids and bases exhibited greater permeabilities than normal salts, while basic salts reacted with the functional groups of GO and thus had lower permeabilities. Finally, an upper limit regarding ion size has been observed for permeation through GO membranes. Expanding on this work, Sun *et al.* reported the transport of alkali and alkaline earth cations through GO membranes

comprised of sheets with nanometer lateral dimensions and sheets with micrometer lateral dimensions as well as a function of temperature.[65] By monitoring the conductivity of the permeate reservoirs, the authors noted that as the dimension of the GO sheets increased, the number of available nanocapillaries decreased, reducing the trans-membrane transport of ions. Upon X-ray photoelectron spectroscopy (XPS), the authors noticed the existence of an additional peak in the spectra associated with cation-π interactions. The authors conclude that the balance between cation-π interactions and ion desolvation determines the ion selective transport through GO membranes. For ions with high solvation energies, the hydration shell will effectively screen and neutralize the ionic charge and thus lower cation-π interactions. This phenomenon was noticed for both the alkali ions as well as the alkaline earth ions, as those ions with low cation-π contributions resulted in faster transport. Furthermore, by varying the temperature from 10 °C to 40 °C, the ion conductivities increases, indicating that temperature promotes ion penetration due to the weakening of the cation-π interactions and the increased thermal motion. Expanding on this work, Sun *et al.* used the differences in ion diffusion due to different interactions with GO to develop energy harvesting devices.[66] The different interactions alter the effective diffusivity of an ion through the GO membrane, resulting in different ionic mobilities. This variation in ionic mobility between anions and cations result in excess concentrations of cations or anions in the source and drain reservoirs, producing a trans-membrane electric potential. It was found that larger variations in ion mobilities between the cations and anions of a salt, introducing a second salt (with a similar cation or anion) into the source, decreasing the effective membrane area, and/or increasing the ion concentration in the source resulted in higher trans-membrane electric potentials.

Finally, Joshi *et al.* investigated the diffusion of ions through micrometer-thick GO membranes and found that cations and anions diffuse through the membranes stoichiometrically in order to maintain charge neutrality.[52] They studied ions with various sizes and charges and found that permeation rates do not exhibit any dependence on charge, as AsO_4^{3-} had the same rate as Mg^{2+} or Cl^-. Furthermore, experiments were repeated with dimethyl sulfoxide (DMSO) as the solvent and noted no permeation through the GO membranes, confirming their earlier conclusions that GO has a special affinity for water.[58] Their investigation on the permeation of ions and neutral molecules through GO membranes resulted

in an upper size limit on permeation such that ions with hydrated radii below 4.5 Å permeated the membrane while larger ions were rejected. By conducting supplementary MD simulations of a GO capillary with a 9 Å slit size, it was suggested that ion permeation is limited to regions where two layers of water can form.

1.4 Ion Selectivity in Carbon Nanotube and Graphene-based Systems

The ability for an ion to enter a hydrophobic carbon nanotube has been linked to the hydration of the ion and electrostatic screening effects at the pore entrance.[67–69] The ability of a solute ion to enter a carbon nanotube pore is dependent on the hydration of the ion; if the size of the ion is smaller than the dimension of the first hydration shell, the ion needs to be partially stripped of the hydrating water molecules in order gain entry to the pore. This occurs at the expense of a dehydration energy penalty.[67] Molecular dynamics simulations have been conducted that explore the dehydration energy barriers of ions entering pores.[70–72] Using a simplified hydrophobic pore model, simulations have shown that ion transport in aqueous solution will occur in equilibrium if the pore radius is greater than 5.3 Å.[73] However, other simulations have shown that ions in an aqueous solution can only pass through carbon nanotubes larger than (7,7) or 4.75 Å.[74] This can play a major role in ion behaviour, as ion selectivity and transport can be attributed to the radial density profiles of water molecules inside the pore that result in their cylindrical formation inside carbon nanotubes.[74] Water molecules have an initial maxima approximately 3.2 Å from the nanotube wall, regardless of its radii, with a series of decreasing maxima until reaching a constant value in the center of the tube. These formations ultimately influence the local ion density positions in the nanotube and the resulting ion transport, as the solvation of the ion in these cylinders is dependent on its coordination number with water.[70] It was found that as the coordination number of the ion with water increased to those of bulk aqueous solutions, the permeation energy barrier and ion selectivity decreases.

Song *et al.* calculated both the 1D and 2D potentials of mean force (PMF) or free energy

profiles *G(r,z)* of various monovalent ions transversing (n,n) CNTs of 13.5 Å length.[70] They note that two-dimensional (2D) PMF profiles provide a more realistic representation of the particle's free energy relative to bulk, thus including it their calculations. They found that different ions have different energy barriers when entering different pores. For example, they found that in a (5,5) CNT, Cl^- ions had the highest energy barrier followed by Na^+ and K^+ ions; however, for (7,7) or (8,8) CNTs, Cl^- ions had the highest energy barrier followed by and K^+ and Na^+ ions. At (9,9), the energy barrier is indistinguishable from each other and hydration of the ions are similar to those found in bulk. Regardless of the variance of energy barriers between different CNTs, they found that Na^+ had the higher energy barrier of the two cations due to its high dehydration energy requirement and low coordination number. Similar results were obtained by Zwolak *et al.*, who showed results show that hydrated ions experience step-wise decreases in solvation energy barriers as less hydrating water molecules are stripped from the ion.[71] It should be noted that the valency of the ion is also important, as higher ion valencies result in higher energy barriers, such that K^+ ions can see a maximum permeation energy barrier of 3 k_BT while Ca^{2+} ions had an energy barrier of 9.5 k_BT in a hydrophobic pore of 10 Å length and 8.5 Å radius.[73]

In addition, electrostatic interactions will tend to be most prominent for small pores and/or low electrolyte concentrations, where the Debye length becomes comparable to the pore radius. This can also induce ionic selectivity due to the repelling of co-ions at the pore entrance.[67] As one increases the ionic strength of a solution, however, the charge at the pore entrance is screened, thus minimizing electrostatic effects.[68,69] This effect increases the potential barrier at the pore entrance, decreasing the permeability of the ions in the channel. However, at higher electric fields, this potential barrier is decreased due to the disruption of water's tetrahedral hydrogen bond network.[72,73] Furthermore, it has been suggested that metallic carbon nanotubes have much stronger screening effects than semiconducting carbon nanotubes when water molecules and ions permeate the nanotubes due to the delocalized π-orbitals of the nanotube's sp^2 graphitic structure.[75]

It is also possible to control ion selectivity by introducing exterior molecules at pore entrances that will sterically and electrostatically select ions.[25,26,68,76] Initial developments in this area consisted of grafting four different types of molecules; a short-chained alkane,

a long-chained alkane, a negatively charged dye molecule and a long polypeptide to the entrance of the CNT pore using basic carbodiimide chemistry.[26] Hindered diffusional transport of methyl viologen (MV^{2+}) and tris(2,2-bipyridyl) dichlororuthenium(II) hexahydrate ($Ru(bpy)_3^{2+}$) dyes through the pores showed that the larger grafted molecules lowered overall dye flux through the various CNTs due to the reduced pore size resulting from steric blocking at the entrance. The only deviation from this conclusion came from the grafted negatively charged dye molecule, which increased the overall flux of the positive dye species through the CNT pore due to Coulombic interactions. Furthermore, from a biological perspective, biotin has been grafted at the CNT pore entrance where the introduction of streptavidin, a protein with an extremely high affinity for biotin, resulted in significant decreases in ionic flux of solute dye molecules due to the steric reduction of the pore entrance by this analyte-receptor complex.[25] The introduction of the biotin at the pore entrance reduced the ionic flux by a factor of 5.5, while the addition of the streptavidin reduced it by a factor of 15. Since this analyte-receptor complex produced an irreversible pore blockage, an additional study investigated the use of a desthiobiotin derivative grafted to the CNT pore entrance to produce a CNT membrane with controlled pore blocking.[76] When the desthiobiotin-CNT membrane is exposed to streptavidin, the streptavidin molecules bind to the desthiobiotin receptor, blocking pore entrances and reduced the flux of methyl viologen. When biotin is introduced to the system, the streptavidin, having a higher affinity for biotin than the desthiobiotin derivative, detaches from the CNT membrane and the flux is restored. These findings are important because they signify the ability to graft biomolecules to the CNT pore entrances that exhibit controllable, reversible pore blocking ability for potential biomedical and drug delivery applications.

As for graphene-based systems, graphene nanopores have shown similar selectivity traits to carbon nanotubes. However, in the case of graphene oxide membranes, there are many arguments regarding the underlying phenomena governing ion permeation and selectivity.[50–55,64,65,77,78] GO membranes at equilibrium with various highly concentrated electrolyte solutions have shown ion transport behaviour similar to bulk.[53] At low salt concentrations, higher-than-bulk cationic transport occurred due to electrostatic attraction from the negatively charged functional groups. This observation extends to partially-reduced GO, where the negatively charged nanochannels still displayed surface-charge-governed ion transporta-

tion at a C/O ratio of 10:1 (compared to conventional GO membranes which have C/O ratios of 2-3:1).[64] This is also supported by other work where high cation rejection rates in GO membranes occurred due to Donnan exclusion principles.[55]

Contradicting these claims, it has been identified that cations and anions diffuse through the membranes stoichiometrically in order to maintain charge neutrality.[52] In this situation, the highly disordered sp^3 oxygen-containing functional groups act as steric blockers and do not contribute to the transport characteristics, only maintaining the interlayer spacing between GO layers and allowing the intercalation of water where the pristine sp^2 graphitic regions provide enhanced flow conditions.[50,52] However, additional studies have challenged this claim and have shown that the sp^3 oxygen-containing functional groups not only interact with the permeating ions and contribute to the selectivity, but also reduce the expected flow enhancement of water through these nanochannels.[51,54,63,65] The presence of sp^3 oxygen-containing functional groups allows one to exhibit controlled rejection of ions and small molecules by suppressing the electrostatic repulsion between individual nanosheets by altering solvent properties such as salt concentration and pH.[54] In addition, the permeation and selectivity of heavy metal salts and ionic salts have been associated to the interaction strength between the metal ions and GO membranes, where the permeation of heavy metal salts are significantly lower than ionic salts due to the tight coordination between the heavy-metal ion and the GO functional groups.[51] In addition, strong acids and bases have exhibited greater permeabilities than normal salts, while basic salts reacted with the functional groups of GO and thus had lower permeabilities. Furthermore, the balance between cation-π interactions with the pristine sp^2 graphitic regions and ion desolvation has also been claimed as the reason for ion selectivity through GO membranes. For ions with high solvation energies, the hydration shell will effectively screen and neutralize the ionic charge and thus lower cation-π interactions, allowing for faster ion permeation.[65]

Finally, an upper limit regarding ion size has been observed for permeation through GO membranes. Joshi *et al.* investigated the permeation of ions and neutral molecules through GO membranes and found that ions with hydrated radii below 4.5 Å permeated the membrane while larger ions were rejected.[52] Similarly, by investigating ionic solutions in other polar solutions such as DMSO and finding no detectable permeation, it was confirmed that

GO have a special affinity for water. By conducting supplementary molecular dynamics simulations of a GO capillary with a 9 Å slit size, it was suggested that ion permeation is limited to regions where two layers of water can form. Despite all these claims, the common conclusion is that two-dimensional graphene nanocapillaries form in the pristine sp^2 graphitic regions with a corresponding capillary force, providing slip flow conditions similar to the water permeation models of carbon nanotubes that allow ion permeation through the GO membranes.[46,50,52,63,65,77,78]

Chapter 2

Sub-Angstrom Ion Selectivity in GO Membranes

2.1 Introduction

The selectivity properties of a membrane are important for separation, desalination, and drug delivery applications as the underlying phenomena governing selectivity and retention can determine membrane performance and feasibility. As it was mentioned in Chapter 1, there are many arguments regarding the phenomena behind ion selectivity through GO membranes.

In order to negate many of the proposed phenomena governing ion selectivity in GO membranes aforementioned in Chapter 1, and to solely focus on the potential steric interactions, the permeation of tris(2,2-bipyridyl) dichlororuthenium(II) hexahydrate $Ru(bpy)_3^{2+}$ and dichlorotris(1,10-phenanthroline)ruthenium(II) hydrate $Ru(phen)_3^{2+}$ ions through GO membranes of various thicknesses is investigated. Both metal complex ions are octahedral with D_3 symmetry consisting of three bidentate heterocyclic ligands in a propeller-like arrangement with similar bond lengths and angles.[79,80] Furthermore, the charge-equivalence of the ruthenium eliminates any potential electrostatic variations between the two ions with the GO membrane due to similar orbital structures. The balance between ion desolvation and cation-π interactions has been claimed as the mechanism for ion selectivity in GO membranes.[65] The first hydration shell contains 15 water molecules in a linear chain formation intercalated between the ligands by hydrogen bonding with one hydrogen per molecule pointing outward.[81,82] This water structure is a result of the electrostatic interactions with the positive ruthenium ion and the apolar ligands. These water molecules

are tightly coordinated within the complex, effectively screening the charge on the ruthenium ion from the pristine sp^2 graphene walls and the sp^3 oxygen-containing functional groups. In addition, the propeller-like configuration of the ligands around the ruthenium ion removes the possibility for planar $\pi - \pi$ stacking with the surface. As a result, the only difference between the two ions is the sub-angstrom size difference resulting from the 6 carbon atoms between the 2, 2-bipyridine and 1, 10-phenanthroline ligands. This creates an ideal system in order to investigate the steric selectivity potential of GO membranes. In the chapter, the ion diffusion rates of these two charge equivalent metal complex ions through GO membranes of various thicknesses is investigated in order to understand the effect of steric interactions on the ion permeation through GO membranes.

2.2 Materials and Methods

GO was synthesized using a modified Hummers method from natural graphite, as reported previously in literature.[83–85] To be brief, graphite flakes (3.0 g, 100 mesh, Sigma-Aldrich) and 1.5 g $NaNO_3$ were mixed with 70 mL concentrated H_2SO_4, stirred for 30 minutes and transferred to a 0 °C ice bath. Following this, 15.0 g $KMnO_4$ was added slowly to keep the temperature below 20°C. After all the $KMnO_4$ was added, the mixture was heated to 35 °C and mixed for 2 hours. The mixture was carefully diluted with 140 mL deionized (DI) water and stirred for another hour. The flask was then removed from the water bath and the mixture was cooled to room temperature, filtered, and washed several times with 5% HCl and DI water. The final solution had a final GO concentration of 3.4 mg/mL. GO membranes were prepared by vacuum filtration of certain volume of diluted aqueous GO solution (0.1 mg/mL) onto polycarbonate (PC) membranes (25 mm diameter, 0.1 μm pore size; Whatman) (Figure 2.1a). A set of GO membranes was made with 0.1, 0.3, 0.5, 0.75, 1.0, and 1.5 mg of GO respectively. Figure 2.1b shows a scanning electron microscopy (SEM) image of a 1.0 mg membrane showing a highly compact layered structure made of individually stacked GO sheets. The GO membrane thickness, determined based on cross-sectional SEM images, increases linearly with GO mass, to a maximum of 3.5 μm at 1.5 mg (Figure 2.1c). The X-ray diffraction (XRD) spectrum of the same 1.0 mg membrane showed a single 2θ peak at 11°, corresponding to an interlayer spacing of 0.7 nm between

stacked GO sheets, which is in agreement with values in previous literature reports.[52,53]

The experimental setup for measuring ion transport through a GO membrane is also shown in Figure 2.1a. For the ease of handling, each GO membrane was sandwiched between two PC filter membranes and two polydimethylsiloxane (PDMS, Sylgard 184, 1:10 catalyst: resin ratio) O-rings with a 4 mm inner diameter, which defined the active membrane area to be 12.6 mm^2. For ion transport measurements, the GO-PC-PDMS assembly was clamped between two polystyrene (PS) cuvettes, which served as the feed and permeate reservoirs. Both reservoirs were filled with 2 mL DI water for 24 hours to effectively hydrate the GO membranes prior to transport studies. At the start of each transport experiment, the DI water in the feed reservoir was replaced by 2 mL 20 mM $Ru(bpy)_3^{2+}$ or $Ru(phen)_3^{2+}$ solution. $Ru(bpy)_3^{2+}$ and $Ru(phen)_3^{2+}$ solutions were made by dissolving tris(2,2-bipyridyl) dichlororuthenium(II) hexahydrate (Sigma-Aldrich) and dichlorotris(1,10-phenanthroline)ruthenium(II) hydrate (Sigma-Aldrich) into DI water respectively. Small aliquots of permeate solution were sampled at various time points over 24 hours. Optical absorbance at 450 nm and 448 nm, measured using a UV-vis spectrometer (PerkinElmer Lambda 25), were used against standard curves (Figure A.1) to determine the concentrations of $Ru(bpy)_3^{2+}$ and $Ru(phen)_3^{2+}$ in the permeate solutions. A reference device with a PC-PDMS assembly clamped between the PS reservoirs was also constructed and ion transport through it was measured to identify the contributions from the supporting PC membranes alone (without GO).

GO was also functionalized with linear polyethylene glycol (PEG-L) using carbodiimide chemistry, which has been successfully used to graft amine-terminated polypeptides and other small molecules onto oxidized carbon nanotubes.[25,26,68] In a typical experiment, 25 mg of GO (approximately 7 mL at [GO] = 3.4 mg/mL) was added to 13 mL of 2-(N-morpholino)ethanesulfonic acid (MES) buffer containing 50 mg amine-terminated linear poly(ethylene) glycol (Poly(ethylene glycol) bis(amine), M_w 20 000, Sigma-Aldrich) as well as equimolar 1-Ethyl-3- (3-dimethylaminopropyl) carbodiimide (EDC) (GBiosciences) and N-Hydroxysuccinimide (NHS) (Alfa Aesar) in excess. The mixture was kept stirring at 25°C for 24 hours. The GO-PEG-L solution was dialyzed against Milli-Q water for 3 days with daily water changes and stored for future use. The fabrication and experimental

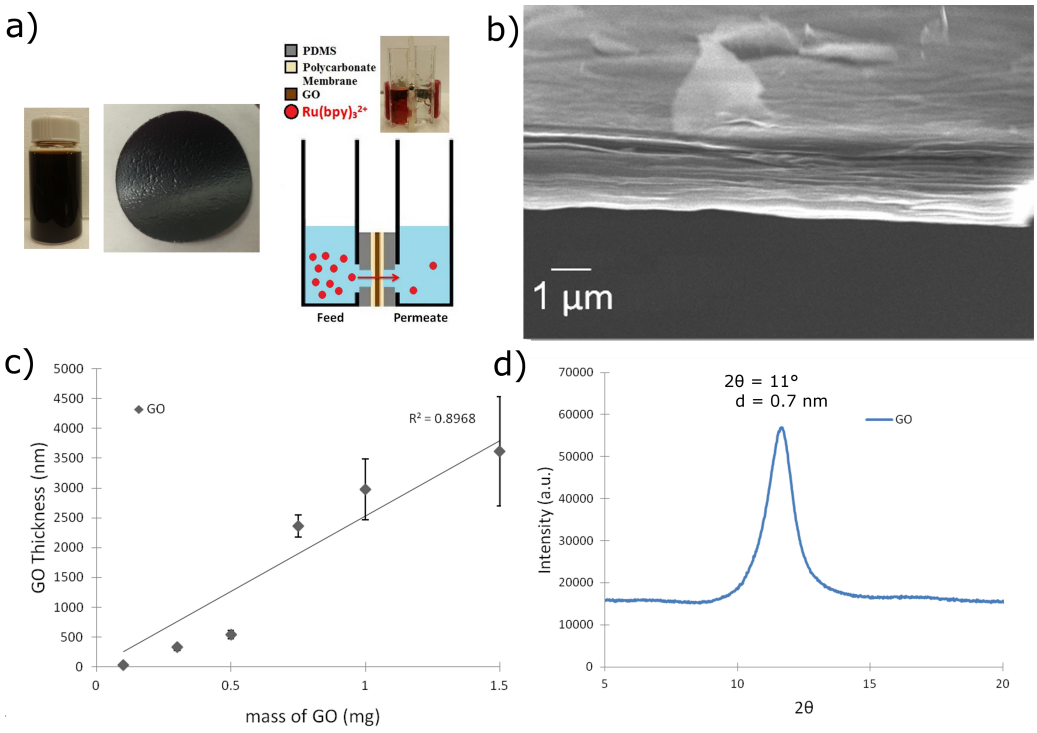

Figure 2.1: GO membrane characteristics. (a) Optical images of a GO aqueous solution and a GO membrane (2.5 cm in diameter) prepared by vacuum filtration. A schematic illustration and an optical image (inset) of the ion transport measurement setup. (b) Cross-sectional SEM image of a 1.0 mg GO membrane. (c) GO membrane thickness vs. GO mass. The line is a linear fit to the data points. Error bars are ±1 standard deviation. (d) X-ray diffraction spectrum of a 1.0 mg GO membrane. Reprinted with permission from Ref. 86

setup of GO-PEG-L membranes were made following the same procedures as above.

2.3 Results and Discussion

2.3.1 Ion Permeation

The diffusive transport of both $Ru(bpy)_3^{2+}$ and $Ru(phen)_3^{2+}$ through various GO membranes was evident, since the ion concentrations in the permeate reservoirs increased steadily over time. Using the permeate ion concentrations measured, the moles of ions permeated through the GO membranes over 24 hours were calculated and plotted in Figure 2.2a and 2.2b. The net flow of ions from the feed to permeate reservoir was driven solely by the concentration difference (ΔC) across the membrane, which was imposed to be 20 mM initially and assumed to be constant (less than 10% change) during the transport measurements. Ion permeation was recorded over a much shorter period (2 hours) on the reference device (without GO), due to the substantially higher net flow of ions observed (Figure 2.2c). By applying linear regression to the data points in Figure 2.2a & 2.2b, and with a known active membrane area, the molar flow rate per unit area ($mmol/hr{\cdot}m^2$), i.e. molar flux (J), was obtained for each membrane and ion for quantitative comparison (Table 2.1). For the 1.5 mg membrane, only the data point at 24 hours was used. The molar fluxes of both $Ru(bpy)_3^{2+}$ (J_{bpy}) and $Ru(phen)_3^{2+}$ (J_{phen}) are inversely proportional to the GO membrane thickness (Figure 2.2d) as predicted by diffusive ion transport. The permeation rate of $Ru(bpy)_3^{2+}$ through GO membranes is on the same order of magnitude as the rate through aligned carbon nanotube membranes.[26]

However, the results shown in Table 2.1 contradict the recently reported findings by Joshi *et al.*, which showed no $Ru(bpy)_3^{2+}$ permeation through GO membranes.[52] In this work, the thickest membrane examined was 3.5 μm, which is considerably thinner than the 5 μm GO films used by Joshi *et al.* In addition, the lateral size of the GO sheets used herein are around 220 nm as determined by dynamic light scattering (DLS, Figure 2.3), which is smaller than the 1 μm sheet size employed in the theoretical calculation of $Ru(bpy)_3^{2+}$ permeation rate by Joshi *et al.* This has shown to be a contributing factor in observing

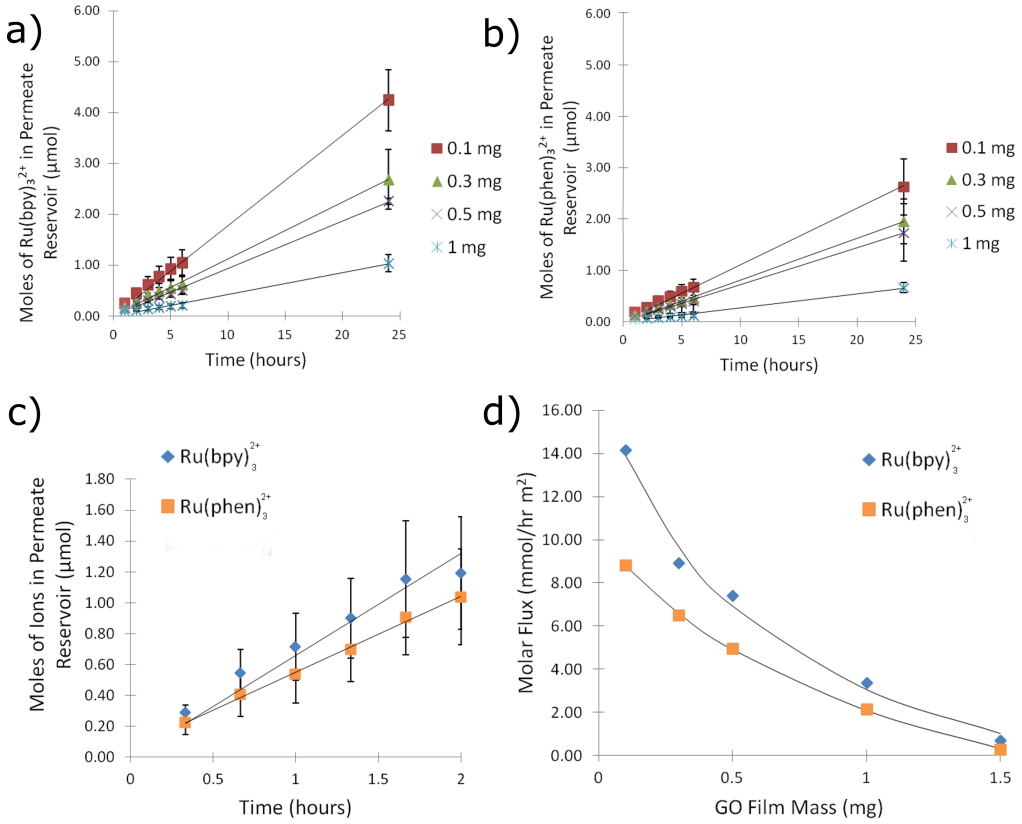

Figure 2.2: Permeation of $Ru(bpy)_3^{2+}$ and $Ru(phen)_3^{2+}$ through GO membranes. (a & b) Moles of $Ru(bpy)_3^{2+}$ and $Ru(phen)_3^{2+}$ transported from the feed to the permeate reservoir through GO membranes of various masses over 24 hours. (c) Moles of $Ru(bpy)_3^{2+}$ and $Ru(phen)_3^{2+}$ permeated through the reference PC membrane (no GO) over 2 hours. Error bars are ± 1 standard deviation and the lines are linear fits. (d) Molar fluxes are inversely proportional (fitted lines) to GO membrane thickness. Reprinted with permission from Ref. 86

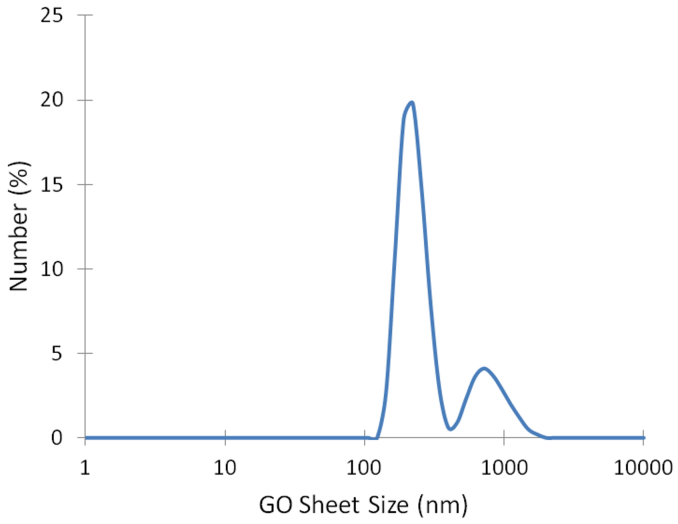

Figure 2.3: The particle size distribution of GO sheets comprising the membranes determined by Dynamic Light Scattering. Reprinted with permission from Ref. 86

Table 2.1: Molar fluxes of $Ru(bpy)_3^{2+}$ and $Ru(phen)_3^{2+}$ through GO membranes of different mass. Reprinted with permission from Ref. 86

	Molar Flux (mmol/hr·m^2)	
GO mass (mg)	J_{bpy}	J_{phen}
0.1	14.16	8.83
0.3	8.91	6.50
0.5	7.43	4.91
1	3.39	2.15
1.5	0.73	0.29

higher molar fluxes through GO membranes, as GO membranes comprising of smaller sheets have more nanochannels available for ion transport.[51,66]

Using the same equation as Joshi *et al.*,

$$MolarFlowRate = D\Delta C\frac{A_{eff}}{L_{eff}} \tag{2.1}$$

where D is the diffusion coefficient of $Ru(bpy)_3^{2+}$ or $Ru(phen)_3^{2+}$ in water (in cm^2/s), ΔC is the concentration gradient across the membrane (in g/cm^3), A_{eff} and L_{eff} are the effective area (cm^2) and length (cm) of the membrane, respectfully. All films have an exposed membrane area of 0.1256 cm^2, thus A_{eff} is 0.1256 cm^2 x d/L = 5.7x10^{-4} cm^2 where L = 220.2 nm (the lateral sheet dimensions determined by Figure 2.3), and d = 1 nm (approximate width of the nanochannels formed by the interlayer spacing of GO). Furthermore, L_{eff} is 220.2 nm x h/d = 6.2x10^{-2} cm for a 1.0 mg film where h is the membrane thickness obtained by SEM as shown Figure 2.1c. For $Ru(bpy)_3^{2+}$ permeation in a 1.0 mg film using a 20 mM feed, one obtains a molar flow rate of 0.432 ng/s or a molar flux of 0.19 mmol/hr·m^2. This results in an enhancement factor of 17 as shown in Table 2.2, which is obtained by dividing the experimentally obtained molar flow rates by the theoretical flow rates.

Table 2.2: Enhancement factors for $Ru(bpy)_3^{2+}$ and $Ru(phen)_3^{2+}$ through GO membranes of different mass. Reprinted with permission from Ref. 86

GO mass (mg)	$Ru(bpy)_3^{2+}$	$Ru(phen)_3^{2+}$
0.1	0.67	0.44
0.3	5	3.82
0.5	6.99	4.89
1	17.53	11.64
1.5	4.5	1.94

Using the Stokes-Einstein equation and the Wilke-Chang correlation, the theoretical Stokes radii and bulk diffusivities of the two ions can be calculated, which are 0.633 nm and 3.872x10^{-10} m^2/s for $Ru(bpy)_3^{2+}$, and 0.664 nm and 3.696x10^{-10} m^2/s for $Ru(phen)_3^{2+}$.[87] The experimentally determined bulk diffusivity of $Ru(bpy)_3^{2+}$ using cyclic voltammetry is

similar to the theoretically calculated value.[88] The experimental molar fluxes are slightly higher than (up to 10 times) the theoretical values. This result indicates that both capillary force[52,58] and low-friction hydrodynamic flow,[58,63,65] which lead to much enhanced (3 orders and higher) ion transport through carbon nanotube and graphene membranes reported in literature, might not be significant in the permeation of the relatively large sized ions through GO membranes, which is studied in this work. A recent study by Wei *et al.* also revealed that the enhancement to water permeation through GO membranes by boundary slip is not significant.[63]

Besides the absolute molar fluxes of the two ruthenium complex ions, the ratio of their flow rates, i.e. J_{phen}/J_{bpy} is investigated. For 0.1 - 1.0 mg GO membranes, the ratios vary from 0.64 to 0.66, while the thicker 1.5 mg GO membrane shows a lower ratio of 0.41±0.07 respectively. Noteworthy is that the two ions, $Ru(bpy)_3^{2+}$ and $Ru(phen)_3^{2+}$, are charge equivalent and structurally similar. They are different by only 5% in bulk diffusivity and 10% in molecular weight, due to the 6 additional carbon atoms contained in the 1, 10-phenanthroline ligands compared to the 2, 2-bipyridine. Consequently, the effects of electrostatic interaction,[51,53,55,64,65] ion desolvation,[65] and capillary force[52,58] on ion permeation should be about the same for the two ions, and cannot account for the significant deviation of J_{phen}/J_{bpy} from unity. Since the pores in a GO membrane are of the same order as those of the ruthenium ions, steric hindrance to ion diffusion should be important and very sensitive to small variations in ion size. The analysis, as presented in the following paragraphs, showed that the large difference in the flow rates of $Ru(bpy)_3^{2+}$ and $Ru(phen)_3^{2+}$ can be explained by sterically hindered diffusion, and the ratios (J_{phen}/J_{bpy}) could give more insight into the pore structures of the GO membranes.

2.3.2 Hindered Diffusion

Three types of pores inside a GO membrane can facilitate ion transport.[44,50,52–54,63,65,89] First, ions can translocate through nanopores created by vacancies, edges and cracks within individual GO sheets. Mechanical handling and/or the harsh chemical exfoliation and oxidation processes involved in GO synthesis can create holes in the graphitic sheets between

1 to 15 nm in lateral size.[44,47–49,89] Second, ions can transport through the voids between individual GO sheets that are formed during the filtration process due to unmatched or misaligned edge geometries, which has been speculated to be only a few GO layers thick.[52] Third, ions can translocate through the 2D nanochannels formed between stacked GO sheets due to the ordered assembly of GO during the filtration process. The first and second types can be modeled as cylindrical pores (Fig. 2.4a) and the third type can be modeled as slits with a width dictated by the GO interlayer spacing, which is reported to be 0.7 to 1.42 nm.[52,53,61]

As previously mentioned in the Introduction, at the nanoscale, hindered diffusion is important for transport in pores of molecular dimensions because the pore dimensions are of the same order as those of a solute molecule.[13] Hindered diffusion takes into account the increased drag on a sphere translating parallel to the pore axis and the velocity of a freely suspended sphere to lag behind the approach velocity of the fluid.[13,14] Furthermore, in addition to geometry, the equilibrium partition coefficient $\Phi(\lambda)$ has been shown to be a function electrostatic interactions between the solute and the pore wall.[15–17]

For $H(\lambda)$ in cylindrical pores, the Bungay and Brenner centreline approximation was used as it has been shown to provide the best estimation for nanofiltration devices and provides a complete correlation for the dimensionless parameter λ (i.e. $0 \leq \lambda \leq 1$).[13,14,18,90]

$$H(\lambda) = \frac{6\pi\Phi}{K_t} \tag{2.2}$$

with

$$K_t = \frac{9}{4}\pi^2\sqrt{2}(1-\lambda)^{-5/2}\left(1 + \sum_{n=1}^{2} a_n(1-\lambda)^n\right) + \sum_{n=0}^{4} a_{n+3}\lambda^n \tag{2.3}$$

The constants for Equation 2.3 can be found in Table 2.3.

For slit nanopore analysis, a cross-sectional average least-squares fit approximation is used since it has been shown to work best for the slit geometry,[14]

$$H(\lambda) = 1 + \frac{9}{16}\lambda\ln\lambda - 1.19358\lambda + 0.4285\lambda^3 - 0.3192\lambda^4 + 0.008428\lambda^5 \tag{2.4}$$

Table 2.3: Constants for the Bungay and Brenner centreline approximation of K_d in cylindrical pores. Reprinted with permission from Ref. 86

a_1	a_2	a_3	a_4	a_5	a_6	a_7
-1.2167	1.5336	-22.5083	-5.6117	-0.3363	-1.216	1.647

Using the Stokes radii of the two ions, $H(\lambda)$ values for $Ru(bpy)_3^{2+}$ (H_{bpy}) and $Ru(phen)_3^{2+}$ (H_{phen}) were calculated for pores up to 5 nm (i.e. h up to 2.5 nm). It is expected that steric hindrance is negligible for pores greater than 5 nm. For cylindrical pores of 1.35-5 nm in size, one obtains H_{bpy} ranging from $2.4x10^{-6}$ to 0.27 and H_{phen} ranging from $8.1x10^{-9}$ to 0.25. For slit pores, one obtains H_{bpy} ranging from 0.014 to 0.507 and H_{phen} ranging from 0.003 to 0.491.

There are some caveats to note when applying those calculations for ions, instead of an uncharged solute. Both $\Phi(\lambda)$ and $K_d(\lambda)$ of Equation 1.5 are known to be modulated by electrostatic interactions. It has been shown that $\Phi(\lambda)$ decreases away from the hard-shell approximation (Equation 1.6) with decreasing ionic strength (defined by the dimensionless parameter κa, where κ is the Debye-Hückel parameter and a is the solute radius) for repulsive electrostatic interactions whereas it increases towards the hard-shell approximation, or becomes even greater than one, for attractive interactions.[15–17] Graphene oxide consists of epoxide and hydroxyl functional groups that populate the basal planes and carboxylic, phenol, and hydroxyl groups along the edges.[47] These negatively charged functional groups have shown surface-charge-governed ion transport characteristics.[53,54,64] As a result, the solute-wall interaction will be attractive and it is expected that $\Phi(\lambda)$ will be equal to or greater than the hard-shell approximation for $Ru(bpy)_3^{2+}$ and $Ru(phen)_3^{2+}$ diffusion. Furthermore, capillary force enacting on the ions in the nanochannel could also make $\Phi(\lambda)$ greater than 1.[52] In addition, for attractive ion-wall interactions, $K_d(\lambda)$ should be slightly lower than the value calculated by centreline approximation, since ions would be drawn off the centerline and experience more drag from the pore wall. Therefore, it is anticipated that the aforementioned calculated $H(\lambda)$ values would be lower than their true values. However, the calculated ratio of H_{phen} to H_{bpy} should be accurate and only dependent on steric hindrance, since contributions from electrostatic interactions are identical for the two charge-equivalent ions.

Figure 2.4c (left panel) shows the theoretical ratio (H_{phen}/H_{bpy}) as a function of pore size for both cylindrical and slit pores. This H ratio is equivalent to the theoretical ratio of J_{phen} to J_{bpy}, as long as the ion concentration gradients across the pores are the same. Regardless of pore shape, the ratio increases rapidly as the pore size increases, which is expected. For pores greater than 3 nm, the ratio approaches unity and any distinction between the permeation of $Ru(bpy)_3^{2+}$ and $Ru(phen)_3^{2+}$ as a result of steric interactions is lost. The theoretical values were further compared to the experimentally measured ratio of flow rates through GO membranes, as plotted in Figure 2.4d (right panel). For GO membranes 0.1 mg up to 1 mg, J_{phen}/J_{bpy} ranged from 0.63 to 0.66, which are consistent with the theoretical ratios for slit pores with a width around 1.45 nm (0.68) and/or cylindrical pores with diameters around 1.75 nm (0.66). Since the highest reported value for the interlayer spacing of fully-hydrated GO in literature is 1.42 nm,[53] it is anticipated that the ion transport pathways in these relatively thin membranes are mainly through holes within GO sheets, voids formed between GO sheet edges, and large slits formed by folds/wrinkles. For the thickest membranes (1.5 mg) tested in this study, the ratio J_{phen}/J_{bpy} dropped significantly to 0.41, indicating that high-resistance pathways consisting of narrower slits (width around 1.375 nm) and/or smaller holes and voids (diameter around 1.61 nm) come into play. It has been shown that the independent stacking of 5 or more GO layers exponentially reduces the effects of micrometer-sized tears and nanometer-sized intrinsic defects on gas permeation through GO.[89] Defects on one GO layer are covered up by subsequent layers unless the defects randomly align. In the 1.5 mg membrane, the effective area and length of the pores formed by aligned porous defects and non-uniform geometries is minimal compared to those of the massive array of slits formed by GO sheet stacking. As a result, ion permeation is primarily limited by the intrinsic interlayer spacing ($\leq$ 1.42 nm) and would follow the theoretical predictions of slit-dominant behaviour.

Further, the possibility to modulate ion permeability of GO membranes through engineering of the interlayer spacing, i.e. slit width, is explored. GO was functionalized with linear polyethylene glycol (PEG-L) using carbodiimide chemistry, and is shown schematically in Figure 2.5a. The grafting of PEG-L onto the lateral surface of the GO sheets, which is shown evidently in the Atomic force microscopy (AFM) image of GO-PEG-L (Figure 2.5b), is expected to increase the interlayer spacing using PEG as the steric blockers to the

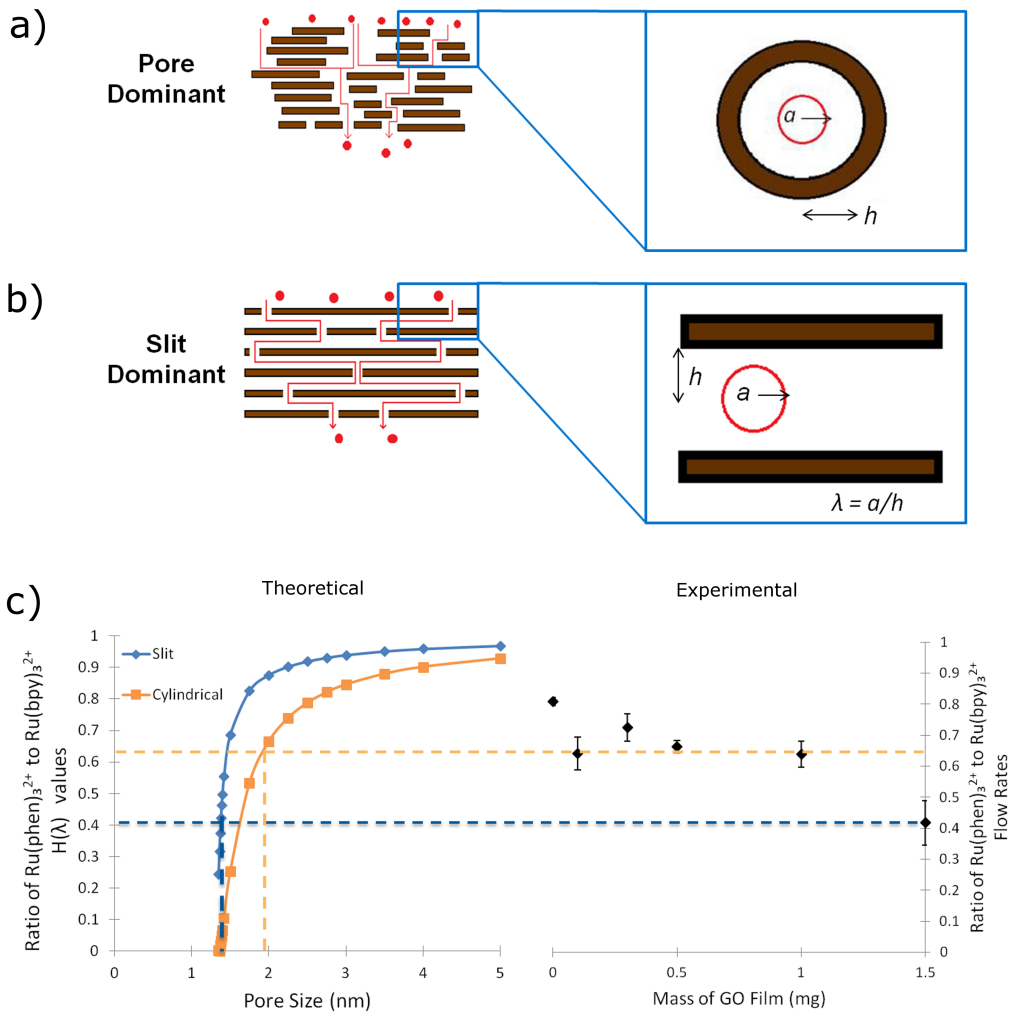

Figure 2.4: Pore structure and steric hindrance to ion diffusion. (a & b) Schematic drawings of the pores in a GO membrane modelled as either cylindrical pores or slits. The ion radius, pore half width, and relative ion size are denoted as a, h, and $\lambda = a/h$, respectively. (c) Comparison of theoretical hindrance coefficient ratios for slit and cylindrical geometries as a function of pore size (left panel) to the experimental ratios of $Ru(phen)_3^{2+}$ to $Ru(bpy)_3^{2+}$ molar flow rates (right panel). The dashed lines correlate the experimentally determined ratios to pore sizes. Reprinted with permission from Ref. 86

stacking of GO. GO-PEG-L membranes were made following the same vacuum filtration procedure. XRD spectra of GO and GO-PEG-L membranes with the same GO mass (1.0 mg) showed a shift in the 2θ peak from 11° to 7.5° (Figure 2.5c), corresponding to an increase in the dry interlayer spacing from 0.7 to 1.1 nm. The SEM image of a GO-PEG-L membrane (Figure 2.5d) showed that it maintained a layered morphology similar to that of pristine GO films. Comparing the thickness of membranes with the same GO mass (1.0 mg), the PEGylation of GO significantly increased the overall membrane thickness from approximately 3.5 μm (GO) to 4.5 μm (GO-PEG-L). Both the XRD and the SEM data support the effective enlargement of interlayer spacing by using PEGylated GO.

Following the same ion transport measurement procedure as done on GO membranes, the moles of $Ru(bpy)_3^{2+}$ and $Ru(phen)_3^{2+}$ permeated through thick 1.5 mg GO-PEG-L membranes over 24 hours were recorded and shown in Figure 2.5e. The molar fluxes of $Ru(bpy)_3^{2+}$ and $Ru(phen)_3^{2+}$ were derived to be 18.71 and 12.74 mmol/hr·m^2 respectively. Compared to the pristine 1.5 mg GO films, the ion permeation rates increased by 2500-4300% despite the increased membrane thickness. This can be attributed to the increased interlayer spacing facilitating $Ru(bpy)_3^{2+}$ and $Ru(phen)_3^{2+}$ permeation. Furthermore, taking the ratio J_{phen}/J_{bpy} for the 1.5 mg GO-PEG-L membrane resulted in a ratio of 0.68, an increase of 0.26 compared to pristine 1.5 mg GO films which had a ratio of 0.41. This result strongly supports the conclusion that thick GO membranes possess a slit-dominant pore structure and steric hindrance is a dominant mechanism governing ion permeation through GO membranes.

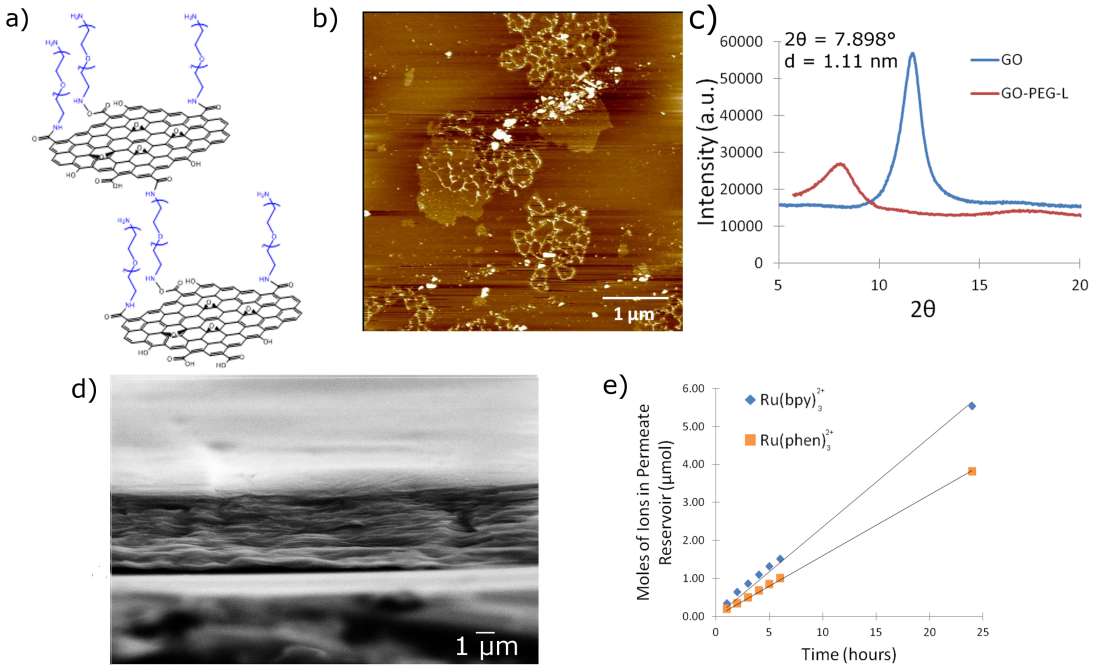

Figure 2.5: Engineering of interlayer spacing by PEGylation of GO. (a) Schematic of GO grafted with linear PEG via carbodiimide chemistry. (b) AFM image of individual GO-PEG-L sheets on a mica substrate. (c) XRD spectra of GO-PEG-L and GO membranes, with the interlayer diffraction peak of GO-PEG-L identified. (d) Cross-sectional SEM image of a 1.0 mg GO-PEG-L membrane. (e) Moles of $Ru(bpy)_3^{2+}$ and $Ru(phen)_3^{2+}$ transported through 1.5 mg GO-PEG-L films over 24 hours. Reprinted with permission from Ref. 86

2.4 Conclusions

In summary, ion transport across GO membranes of various thicknesses, made by vacuum filtration of GO aqueous solutions was investigated. The diffusive transport rates of two charge-equivalent and structurally similar ruthenium complex ions, $Ru(bpy)_3^{2+}$ and $Ru(phen)_3^{2+}$, with a sub-angstrom size difference, through GO membranes are distinguishable. Taking the ratio of the molar fluxes of the two ions (J_{phen}/J_{bpy}) allowed the identification regarding the effect of steric interactions on ion transport, among the many other mechanisms proposed in literature, such as electrostatic interactions, capillary force, boundary-slip enhanced water flow, ion desolvation, etc. Furthermore, by correlating the experimentally determined ratio J_{phen}/J_{bpy} with the theoretically calculated ratio of hindrance coefficients (H_{phen}/H_{bpy}) in cylindrical and slit pore models, one is able to gain some insight into the pore structures of GO membranes. Analysis suggests that ion transport is mostly facilitated by large pores (greater than 1.75 nm in diameter) in the relatively thin GO membranes, while slits formed by GO stacking (less than 1.42 nm in width) become dominant only in thick membranes, such as the 3.5 μm membranes (1.5 mg) shown in this work. By grafting PEG molecules to the lateral plane of GO sheets, membranes with enlarged interlayer spacing were engineered, which showed drastically increased ion transport rates and lower distinction among the two ruthenium ions, consistent with the prediction by the slit-dominant steric hindered diffusion model. This work expands the versatility of GO membranes for molecular sieving and separation applications by adding another class of molecules in addition to alkali and alkaline earth ions and the larger organic dyes already reported. Furthermore, findings could give guidance to the rational design of GO membranes for high-precision ion selectivity and molecular sieving.

Chapter 3

Optimizing Transport and Selectivity Characteristics of PEGylated GO Membranes

3.1 Introduction

As it was briefly shown in Chapter 2, the functionalization of GO can modulate ion permeability and alter the ion selectivity characteristics of GO membranes. This was seen in the ion permeation rates of two charge equivalent metal complex ions, $Ru(bpy)_3^{2+}$ and $Ru(phen)_3^{2+}$. By functionalizing the GO sheets with PEG-L via carbodiimide chemistry, the interlayer spacing between GO sheets was expanded, reducing the intrinsic selectivity properties of pristine GO.

There has been many covalent and non-covalent approaches to functionalizing graphene and GO for various applications.[56,91] For example, using a covalent approach, one can utilize nucleophilic substitutions and ring-opening reactions between the epoxy groups of GO with amine groups, which has successfully attached amines, amino acids, amine-terminated biomolecules, polymers and ionic liquids to the surface of GO.[92–94] In addition, by utilizing electrophilic substitution reactions, one can functionalize the graphitic sp^2 surface. This is generally performed using diazonium salts, which have also been used on carbon nanotubes to increase their solubility, decrease intermolecular cohesion, and/or modulate ion permeation in CNT membranes.[95–97] Furthermore, reacting the carboxylic acid groups on the edges of GO sheets with amine or isocyanate groups result in condensation reactions, forming amide and carbamate bonds (with the loss of water and carbon dioxide, respect-

fully). From a non-covalent approach, one can use $\pi - \pi$, cation - π, anion -π, and Van der Waals interactions in order to functionalize graphene and GO.[56,91,98]

Regardless of the chemistry used to functionalize GO, the presence of small molecules, biomolecules or polymers can result in modulation of ion permeation rates and selectivity. In this chapter, GO membranes are functionalized with different molecular weight PEG-L molecules via carbodiimide chemistry in order to expand upon the earlier work of Chapter 2 and optimize ion transport and ion selectivity characteristics.

3.2 Materials and Methods

GO was functionalized with linear poly(ethylene) glycol (PEG-L) using conventional carbodiimide chemistry. For linear PEG functionalization, 25 mg of GO (approximately 4 mL at [GO] = 6.1 mg/mL) was added to 36 mL MES buffer containing 50 mg amine-terminated linear poly(ethylene) glycol of desired molecular weight (Poly(ethylene glycol) bis(amine), M_w = 20 000, M_w = 6 000, or M_w = 3 000, Sigma-Aldrich) as well as equimolar EDC (GBiosciences) and NHS (Alfa Aesar) in excess. The mixtures were kept stirring at 25 °C for 24 hours. The GO-PEG-L# solutions (L20, L6, and L3 for M_w = 20 000, M_w = 6 000, and M_w = 3 000, respectfully) were dialyzed against Milli-Q water for 3 days with water changes every 12 hours and stored for future use. GO-PEG-L# membranes were prepared by vacuum filtration of certain volume of diluted aqueous GO-PEG-L# solution (0.1 mg/mL) onto PC membranes (25 mm diameter, 0.1 μm pore size; Whatman).

For Fourier transform infrared spectroscopy (FTIR), 1 mL of GO and functionalized GO solutions (0.61 mg/mL) were freeze dried for 24 hours prior to experiments. Solid GO and functionalized GO were finely ground with KBr (Sigma Aldrich) and compressed into thin pellets. FTIR spectra were collected using a Bruker Tensor 37 FTIR spectrometer from 4000 cm^{-1} to 600 cm^{-1}. For Thermal Gravimetric Analysis (TGA) measurements, 5 mL of GO and functionalized GO solutions (0.61 mg/mL) were freeze dried for 24 hours prior to experiments. Solid GO and functionalized GO samples were placed in a SDT Q600 V8.2 Build 100 thermogravimetric analyzer in an alumina pan with an air flow rate of 100

mL/min. Temperature parameters were set from 25 to 1000 °C with a ramp rate of 10 °C/min.

The experimental setup and measuring procedure is identical to the protocol outlined in Chapter 2. To briefly re-iterate, each functionalized membrane was sandwiched between two PC filter membranes and two PDMS O-rings with a 4 mm inner diameter, which defined the active membrane area to be 12.6 mm^2. For ion transport measurements, the GO-PC-PDMS assembly was clamped between two polystyrene cuvettes, which served as the feed and permeate reservoirs. Both reservoirs were filled with 2 mL DI water for 24 hours to effectively hydrate the GO-PEG-L# membranes prior to transport studies. At the start of each transport experiment, the DI water in the feed reservoir was replaced by 2 mL 20 mM $Ru(bpy)_3^{2+}$ or 20 mM $Ru(phen)_3^{2+}$ and small aliquots of permeate solution were sampled at various time points over 6 hours. Optical absorbance at 450 nm and 448 nm was used to determine the concentration of $Ru(bpy)_3^{2+}$ and $Ru(phen)_3^{2+}$ in the permeate solutions.

3.3 Results and Discussion

3.3.1 Membrane Characterization

Figure 3.1a-c shows SEM images of 1.0 mg GO-PEG-L# membranes consisting of a highly compact layered structure, indicating functionalization does not alter the overall membrane structure relative to pristine GO. However, overall thicknesses did not scale according to molecular weight, as average membrane thicknesses were 3 μm, 4.4 μm, and 3.8 μm for the L3, L6, and L20 membranes, respectfully (Figure 3.1a-c). Since the polymers are grafted to the COOH groups which populate the edges of the GO sheets, the voids formed between GO sheet edges can potentially be blocked. The PEG-L molecules consist of one NH_2 group at each chain end, indicating four possibilities for amide bond formation; between two COOH groups on adjacent individual GO sheets, cross-linking them together in the lateral direction or between two adjacent sheets in the vertical direction, between two COOH groups on the same GO sheet (depending on the distance of adjacent COOH

groups on an individual GO sheet), or only one NH_2 group reacting to form an amide bond and the other remaining a lone NH_2 group. This creates an intricate web of potential stacking configurations for the GO to take during the initial membrane setup, altering the overall pathway taken by the ions (relative to pristine GO) and thus changing the transport and selectivity characteristics. This could explain the minor differences in L3, L6, and L20 membrane thicknesses as seen in Figure 3.1.

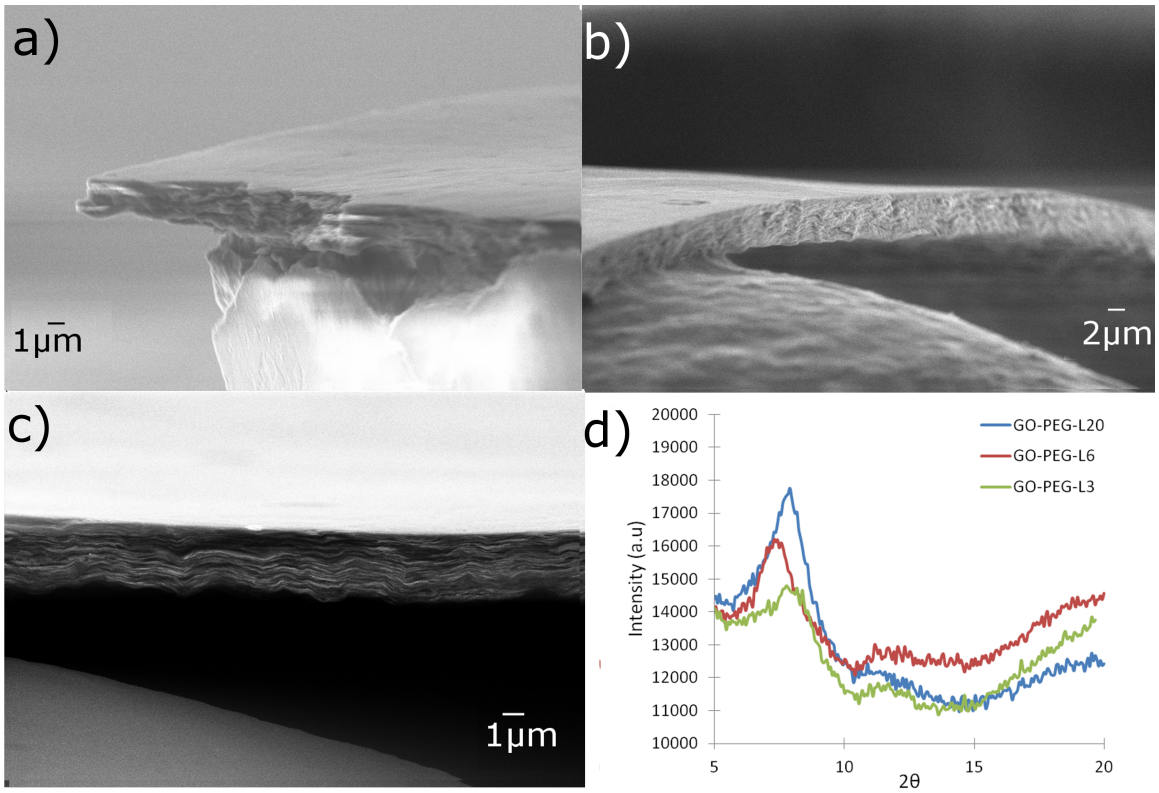

Figure 3.1: GO-PEG-L# membrane characteristics. Cross-sectional SEM image of (a) GO-PEG-L3, (b) GO-PEG-L6, and (c) GO-PEG-L20 membrane. (d) X-ray diffraction spectra of GO-PEG-L# membranes.

It can be seen from the XRD spectra that all GO-PEG-L# films consist of a major peak located around 7.6° (1.13 nm) regardless of molecular weight (Figure 3.1d), suggesting that the interlayer spacing is independent of molecular weight.[99] The bulk radius of gyration $R_{g,bulk}$, which refers to the dimensions of the polymer chain, scales with increasing molecular

weight from 2.26 nm (M_w = 3 000) to 6.21 nm (M_w = 20 000) (see Appendix B.3.1), suggesting there should be a significant difference in the L3, L6, and L20 XRD spectra if PEG-L exhibits three-dimensional bulk behaviour in the membranes. However, since this is not observed in Figure 3.1d, and the interlayer spacing is on the same order as the radius of gyration, the behaviour of grafted PEG-L on GO as a result of confinement must be investigated.

Recent developments have investigated the two-dimensional configurations of polymers and Deoxyribonucleic acid (DNA) in both de Gennes[100,101] and Odijk[102] regimes for slit-like confinements in order to optimize micro and nanofluidic platforms.[103–108] By confining a polymer in a slit geometry, the reduction in the z-direction increases the local monomer density, which increases the excluded-volume interactions within the chain. To counter this, the two-dimensional size of the polymer increases along the x-y plane into the slit.[105,106,108] The magnitude of this effect is determined by the degree of confinement experienced by the polymer. The degree of confinement and the governing confinement regime for the polymers in the GO membranes can be determined by relating $R_{g,bulk}$ to the interlayer spacing d by the following equation.[104]

$$C = \frac{R_{g,bulk}}{d} \tag{3.1}$$

For the confinement to be classified in the de Gennes regime, C has to be $1 < C \ll R_{g,bulk}/l_p$, while the Odijk regime occurs when $d \leq l_p$, where l_p is the persistence length of the polymer (0.38 nm for PEG[109]). The PEG-L polymers have C values of 2.03, 3.03, and 6.12 (for L3, L6, and L20, respectfully), indicating that the GO-PEG-L# membranes fall in the de Gennes regime. The de Gennes regime models a polymer as a string of blobs with diameter equal to the slit height d that follow a two-dimensional self-avoiding walk whose equilibrium size, diffusivity, and relaxation time follow scaling predictions.[100,101,105] In addition, the radius of gyration can be decomposed into its planar ($R_\parallel$) and normal ($R_\perp$) components in order to investigate the effect of confinement on the dimensions of the confined polymer chains.[101] The planar component can be related to the radius of gyration by the following equation,[104,106]

$$\frac{R_{\parallel}}{R_{g,bulk}} \sim \left(\frac{R_{g,bulk}}{d}\right)^{\beta} \tag{3.2}$$

$$\frac{R_{\parallel}}{R_{g,bulk}} \sim C^{\beta} \tag{3.3}$$

where β is the scaling factor associated with the confinement of the polymer chain.

For confined polymers in the de Gennes regime, it has been shown that the radius of gyration exhibits anisotropy such that $R_{\parallel} > R_{\perp}$.[104–106] In this case, $R_{\parallel}$ stretches and extends into the slit along the x-y direction according to Equation 3.3 while $R_{\perp}$ scales linearly and occupies all the available space in the slit for values of $1/C < 2$.[104] The values of $1/C$ in this work fall below this limit, indicating that the confinement in the z-direction results in an extension in the x-y plane (Appendix B.3.1). This can be supported by the XRD results, which show similar interlayer spacings for L3, L6, and L20 membranes.

For the evaluation of $R_{\parallel}$ using Equation 3.3, the scaling factor β has been evaluated for a variety of DNA and single polymers across a broad range of C, and small differences have been obtained resulting from different degrees of confinement C and number of monomers N in the polymer chain[103–108] As a result, the theoretical evaluation of $\beta = 0.25$[106] is used to calculate $R_{\parallel}$. Evaluating Equation 3.3 gives 2.73 nm, 4.52 nm, and 10.88 nm for L3, L6, and L20, respectfully. It should be noted that some publications define Equation 3.3 differently such that they include the relationship $R_{\parallel,bulk} = \sqrt{2/3}R_{g,bulk}$.[105,108] This is not significant to this work as all calculations would scale accordingly.

The FTIR spectra of GO (Figure 3.2a) exhibits differences due to the addition of PEG-L. GO exhibits the following peaks; 3500 cm^{-1} attributed to the hydroxyl stretching of the C-OH groups; 1630 cm^{-1} attributed to carbonyl stretching of the COOH groups, and a weak peak at 1100 cm^{-1} attributed to the stretch of the C-O-C groups. The PEGylation of GO introduced additional peaks (Figure 3.2a); 2880 cm^{-1} attributed to the asymmetric/symmetric stretching of the C-H groups; 1460 and 1352 cm^{-1} attributed to the asymmetric/symmetric bending of the C-H groups, as well as 952 and 840 cm^{-1} attributed to the rocking of the C-H groups or the out-of-plane bending of hydrogen bonded O-H groups.

It should also be noted that peaks associated with the vibrational modes of C-N and N-H groups tend to fall in the 1650 - 1100 cm^{-1} range, which makes the identification of these modes difficult since PEG-L contains more methylene groups in the polymer chain than C-N and N-H bonds associated with the polymer ends and/or amide bonds formed during the reaction. Furthermore, since the relative intensities of the 2880, 1100, 952, and 840 cm^{-1} peaks scaled with increasing molecular weight, it can be deduced that these are associated with the polymer chain (Figure B.1).

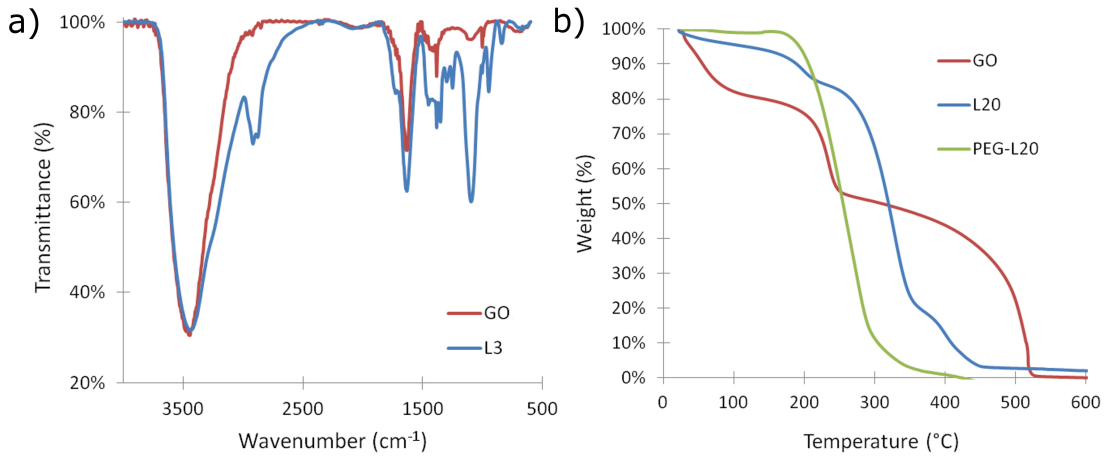

Figure 3.2: (a) FTIR spectra of pristine GO and GO-PEG-L3 membranes. (b) TGA analysis GO-PEG-L# membranes.

Figure 3.2b shows the thermal decomposition of GO, pure PEG-L and PEGylated GO samples. GO continuously loses weight from ambient temperature to 130 °C, which is associated with the loss of adsorbed water molecules covering the surface. Subsequent decompositions occur at 180 - 220 °C and 500 °C, which are attributed to the pyrolysis of labile O_2 functional groups and the thermal decomposition of the carbon skeleton, respectfully.[47] PEGylated GO consists three decompositions; 180 - 220 °C, 280 - 330 °C, and 400 - 450 °C. These are attributed to the pyrolysis of labile O_2 functional groups, the decomposition of the ethylene chain, and the decomposition of the carbon network of GO. Furthermore, since the relative magnitude of the weight loss from 280 - 330 °C in GO-PEG-L samples increase with molecular weight (Figure B.2), it can be deduced that

this is the decomposition of PEG-L grafted to GO. Pure PEG-L is shown for reference and undergoes a single decomposition from 180 °C to 330 °C due to the decomposition of the ethylene oxide chain.

3.3.2 Ion Permeation through GO-PEG-L membranes

Ion concentrations of both $Ru(bpy)_3^{2+}$ and $Ru(phen)_3^{2+}$ were recorded through various GO-PEG-L# membranes and the moles of ions permeated through the GO-PEG-L# membranes over 6 hours are plotted in Figures 3.3a & 3.3b. By applying linear regression to the data points in Figures 3.3a & 3.3b, and with a known active membrane area, the molar flow rate per unit area (mmol/hr·m^2), i.e. molar flux (J), was obtained for each membrane and ion for quantitative comparison (Table 3.1).

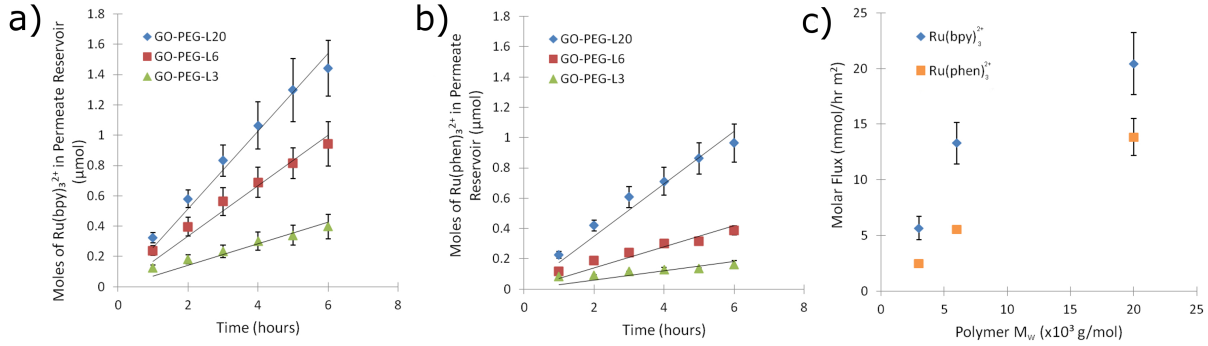

Figure 3.3: Permeation of $Ru(bpy)_3^{2+}$ and $Ru(phen)_3^{2+}$ through GO-PEG-L# membranes. (a) Moles of $Ru(bpy)_3^{2+}$ transported from the feed to the permeate reservoir through 1.0 mg GO-PEG-L# membranes over 6 hours. (b) Moles of $Ru(phen)_3^{2+}$ transported from the feed to the permeate reservoir through 1.0 mg GO-PEG-L# membranes over 6 hours. Error bars are ±1 standard deviation and the lines are linear fits. (c) Molar fluxes of $Ru(bpy)_3^{2+}$ and $Ru(phen)_3^{2+}$ are proportional to polymer molecular weight M_w.

The functionalization of PEG-L onto GO increased the $Ru(bpy)_3^{2+}$ and $Ru(phen)_3^{2+}$ flux through GO-PEG-L# membranes compared to pristine GO up to ~800%. Furthermore, the molar fluxes of $Ru(bpy)_3^{2+}$ and $Ru(phen)_3^{2+}$ through PEGylated GO membranes increased with increasing molecular weight (Figure 3.3c). This could be a combination of

Table 3.1: Molar fluxes of $Ru(bpy)_3^{2+}$ and $Ru(phen)_3^{2+}$ through 1.0 mg GO and GO-PEG-L# membranes

	Molar Flux (mmol/hr·m^2)		
Membrane	J_{bpy}	J_{phen}	J_{phen}/J_{bpy}
GO	2.50	1.71	0.68
L3	5.65	2.44	0.43
L6	13.29	5.54	0.41
L20	20.44	13.83	0.67

three factors. First, the PEGylation procedure alters the overall pathway for ion transport and expands the porous structure, which was shown in the XRD spectra in Figure 3.1d. Secondly, it has been shown that PEG-L maintains a partial helical structure in solution that induces hydrophobicity and scales with polymer length.[110–113] This would reduce any enhancement-impairing interactions due to interactions with the oxygen in the PEG-L chain. Finally, any confinement along the x-y plane would reduce the influence of any enhancement-impairing sp^3 oxygen-containing functional groups on the GO sheet.[51,54,63,65] These factors would promote enhanced hydrodynamic flow[46,50,52,63,65,77,78] and allow a higher magnitude of $Ru(bpy)_3^{2+}$ or $Ru(phen)_3^{2+}$ flux through the membrane. This is opposite to the findings of Majumder *et al.* who observed decreasing $Ru(bpy)_3^{2+}$ flux through CNTs as the length of the grafted molecule increased.[26] In the case of CNTs, this was attributed to the hydrophobic alkanes reducing the pore dimensions and increasing the overall hydrophobicity of the pore entrances.

Recalling the hindered diffusion models used in Chapter 2, J_{phen}/J_{bpy} ratios for GO-PEG-L# membranes are tabulated in Table 3.1 to relate the size of the intercalated PEG-L to the steric selectivity properties of the GO membranes. A J_{phen}/J_{bpy} value of one indicates no difference in hindrance between the two ions, while a value less than one indicates a difference in hindrance (and thus selectivity).

Analyzing the results, the PEGylation of GO with L20 does not alter the ion selectivity characteristics despite increased molar flux compared to the pristine GO membrane, as both membranes have a ratio of 0.67. This suggests that the L20 polymer opens up the membrane, allowing a higher molar flux (∼800%) without compromising ion selectivity

(relative to pristine 1.0 mg GO membranes). It should be noted that in Chapter 2, 1.5 mg GO-PEG-L20 membranes were utilized to compare the effects of functionalization on the interlayer spacing as ion permeation through the thicker 1.5 mg GO membranes was primarily limited by the intrinsic interlayer spacing ($\leq$ 1.42 nm) and followed the theoretical predictions of slit-dominant behaviour.[86] In this chapter, the use of 1.0 mg membranes does not remove the contributions from holes within GO sheets, voids formed between GO sheet edges, and large slits formed by folds/wrinkles. In the L3 and L6 membranes, although the molar fluxes are slightly higher compared to pristine GO ($\sim$150-225% for L3 and $\sim$325-530% for L6), the hindrance ratio is also reduced to 0.41 - 0.43. This suggests that for these two membranes, PEGylation closes some of the larger pores and potential defects and forces the ions to travel through higher resistance pathways as their ratios are similar to the 1.5 mg pristine GO ratio (0.41) obtained in Chapter 2. Finally, it should be noted that the results obtained in Figure 3.3c will not affect the J_{phen}/J_{bpy} results of Table 3.1 since any non-steric interactions with the polymer chain and the GO sheet are expected to be similar for both ions.

Therefore, when applications require high ion transport rates, L20 membranes should be utilized instead of pristine GO as they showed the highest molar fluxes reported without compromising intrinsic GO selectivity properties, while L6 membranes should be used in applications where increased selectivity properties are desired. If both high molar flux and increased selectivity properties are desired, it is recommended based on the data in Figure 3.3 and Table 3.1 that L6 membranes are utilized instead of pristine GO.

3.4 Conclusions

In summary, ion transport across PEGylated GO membranes was investigated in order to optimize ion transport by engineering the pore structure of GO membranes. The addition of PEG-L altered the nanofluidic channel geometry, increasing the overall ion flux relative to pristine GO membranes.

The molar fluxes through 1.0 mg PEGylated GO membranes were enhanced compared to

pristine GO and scaled with molecular weight. The enhanced molar fluxes through these PEGylated GO membranes was attributed to pore reconfigurations, ion-polymer, and ion-graphene interactions within the membrane. Analysis of J_{phen}/J_{bpy} ratios for the 1.0 mg membranes determined that the shorter polymers tightened up and closed the larger pores, increasing the flux and selectivity while the longer polymers opened up the overall porous structure, increasing flux but not altering the observed selectivity. Based on the results herein, when applications require high ion transport rates, L20 membranes should be utilized as they showed the highest molar fluxes reported without compromising intrinsic selectivity properties, while L6 membranes should be used in applications where increased selectivity properties are desired. If both high molar flux and selectivity properties are desired, it is recommended based on the data in Figure 3.3 and Table 3.1 that L6 membranes are utilized.

Chapter 4

Design of Temperature-Responsive GO Membranes

4.1 Introduction

As it was shown in Chapter 3, GO was successfully functionalized with linear poly(ethylene) glycol of different molecular weights. The molar fluxes through these PEGylated GO membranes were enhanced compared to pristine GO that scaled with molecular weight. This was attributed to a combination of pore reconfigurations and hydrophobic changes within the membranes. Expanding upon Chapter 3, this chapter will investigate the functionalization of GO with molecules that respond to external stimuli (e.g. thermal, light, magnetic, pH) to create smart GO membranes with in-situ control of permeation and selectivity characteristics.

Poly(*N*-isopropylacrylamide) (PNIPAm) is a thermosensitive, water-soluble polymer that undergoes an abrupt structural change at its Lower critical solution temperature (LCST) around 32 °C, exhibiting hydrophobic behaviour.[114–116] This structural change and decrease in solubility is due to the disordering of the water-amide hydrogen bonds and the presence of intermolecular polymer-polymer hydrogen bonds.[114,117] However, in dilute aqueous solutions, intramolecular polymer-polymer bonds form instead since neighbouring polymer chains are far away and intermolecular polymer-polymer bonds cannot replace the polymer-hydrogen bonds, resulting in a coil-to-globular transition. Since the LCST of PNIPAm is in the temperature range of the human body and the abrupt change in solubility results in the expulsion of the surrounding aqueous media, PNIPAm has been investigated as a possible material for therapeutic and diagnostic applications.[118–123] In this chapter, GO is

functionalized with PNIPAm in order to create thermo-sensitive membranes.

4.2 Materials and Methods

GO was functionalized with poly(*N*- isopropylacrylamide) (PNIPAm) using conventional carbodiimide chemistry. For PNIPAm functionalization, 25 mg of GO (approximately 4 mL at [GO] = 6.1 mg/mL) was added to 36 mL MES buffer containing 25 mg amine-terminated Poly(N-isopropylacrylamide), M_n = 4 500, Sigma-Aldrich) as well as equimolar EDC (GBiosciences) and NHS (Alfa Aesar) in excess. The mixtures were kept stirring at 25 °C for 24 hours. The GO-P solutions (L20, L6, and L3 for M_w = 20 000, M_w = 6 000, and M_w = 3 000, respectfully) were dialyzed against Milli-Q water for 3 days with water changes every 12 hours and stored for future use. GO-P membranes were prepared by vacuum filtration of certain volume of diluted aqueous GO-P solution (0.1 mg/mL) onto PC membranes (25 mm diameter, 0.1 μm pore size; Whatman).

The Fourier transform infrared spectroscopy (FTIR) and Thermal Gravimetric Analysis (TGA) measurement procedures are identical to the protocols outlined in Chapter 3. To briefly re-iterate, 1 mL of GO and GO-P solutions (0.61 mg/mL) were freeze dried for 24 hours prior to experiments, finely ground with KBr, compressed into thin pellets, and FTIR spectra were collected from 4000 cm^{-1} to 600 cm^{-1}. For TGA measurements, 5 mL of GO and GO-P solutions (0.61 mg/mL) were freeze dried, placed in a SDT Q600 V8.2 Build 100 thermogravimetric analyzer in an alumina pan with an air flow rate of 100 mL/min, and set from 25 to 1000 °C with a ramp rate of 10 °C/min.

Furthermore, the experimental setup and measuring procedures are identical to the protocols outlined in Chapters 2 & 3. For elevated temperature experiments, each device was covered with paraffin film to reduce evaporation and placed in an oven at the preset temperature. Reservoir temperatures were confirmed by placing a thermometer into reservoirs during sampling.

4.3 Results and Discussion

4.3.1 Membrane Characterization

Figure 4.1a shows a SEM image of a 1.0 mg GO-P membrane consisting of a highly compact layered structure, indicating functionalization does not alter the overall membrane structure relative to pristine GO. Similar to the results of Chapter 2, increasing the mass of the GO-P membrane linearly increased the overall thickness of the membrane (Figure 4.1b).

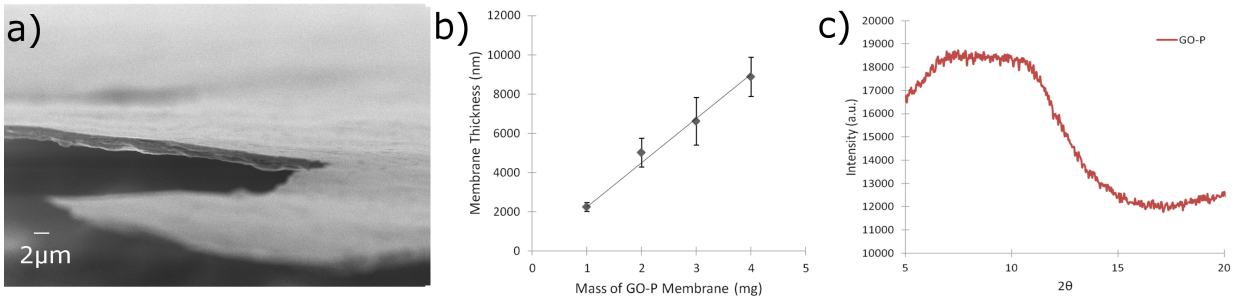

Figure 4.1: GO-P membrane characteristics. (a) Cross-sectional SEM image of 1.0 mg GO-P membrane. (b) GO-P membrane thickness vs. mass. The line is a linear fit to the data points. Error bars are ±1 standard deviation. (c) X-ray diffraction spectrum of GO-P membrane.

XRD spectra of dry GO-P membranes showed a broad peak from 7° to 11° (Figure 4.1c). Using a peak fitting program in MATLAB,[124] this peak can be deconvoluted into two major peaks located at 7.36° and 10.02°, corresponding to interlayer spacings of 1.20 nm and 0.88 nm, respectfully (Figure B.3, Table B.1). This suggests that GO-P membranes contain domains of pristine GO as well as domains with expanded interlayer spacings resulting from PNIPAm functionalization. Following the de Gennes confinement theory for PEGylated membranes in Chapter 3, the evaluation of Equations 3.1 and 3.3 result in 1.86 and 2.45 nm for C and $R_{\|}$, respectfully (Appendix B.3.2). Upon comparison with the results obtained for the GO-PEG-L# membranes, it can be seen that PNIPAm experiences less confinement in the GO membranes and does not extend into the interlayer spacing as

much as the smallest PEG-L polymer (2.03 for L3). This supports the notion that GO-P membranes contain domains of pristine GO as well as domains with expanded interlayer spacings resulting from PNIPAm functionalization.

The FTIR spectra of GO (Figure 4.2a) exhibits differences due to the addition of PNIPAm. As mentioned in Chapter 3, GO exhibits the following peaks; 3500 cm^{-1} attributed to the hydroxyl stretching of the C-OH groups; 1630 cm^{-1} attributed to carbonyl stretching of the COOH groups, and a weak peak at 1100 cm^{-1} attributed to the stretch of the C-O-C groups. The functionalization of GO with PNIPAm has peaks located at 1630, 1550, 1460, 1380, and 1130 cm^{-1} associated to the carbonyl, amide, and methyl moieties in the monomer, respectfully (Figure 4.2a). Furthermore, a small peak exists at 680 cm^{-1} attributed the stretching of the thiol group in the polymer chain.

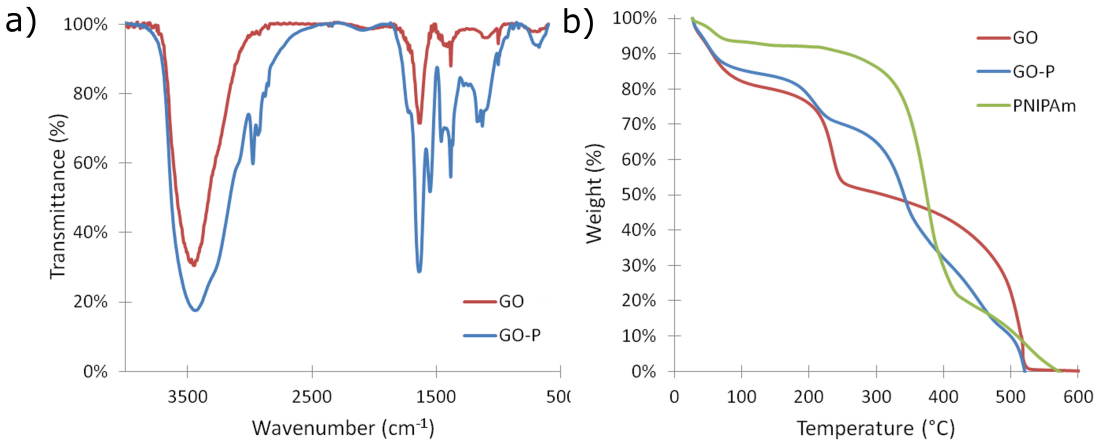

Figure 4.2: (a) FTIR spectra of pristine GO and GO-P membranes. (b) TGA analysis GO-P membranes.

Figure 4.2b shows the thermal decomposition of GO, pure PNIPAm and GO-P samples. GO continuously loses weight from ambient temperature to 130 °C, which is associated with the loss of adsorbed water molecules covering the surface. Subsequent decompositions occur at 180 - 220 °C and 500 °C, which are attributed to the pyrolysis of labile O_2 functional groups and the thermal decomposition of the carbon skeleton, respectfully.[47] GO-P samples consist of two decompositions: 180 - 220 °C attributed to the pyrolysis

of labile O_2 functional groups, and 280 - 500 °C attributed to the decomposition of the PNIPAm chain. Pure PNIPAm is also shown for reference.

4.3.2 Ion Permeation through GO-P membranes

Ion concentrations in the permeate reservoir were recorded through GO-P membranes for two different temperatures: T < LCST (32 °C) and T > LCST. This corresponded to an experimental temperature of 25 °C (Figure 4.3a) & 45 °C (Figure 4.3b). The molar flux for the GO-P membranes studied in this work at each temperature, and the corresponding temperature ratio, i.e. J_{45}/J_{25} is shown in Table 4.1 for quantitative comparison. These values are corrected for the effect of temperature on the molar extinction coefficient, which showed an absorbance decay of 3.74% over the course of the experiment (see Appendix A.3). Similar to pristine GO membranes in Chapter 2, the molar flux of $Ru(bpy)_3^{2+}$ is inversely proportional to the membrane thickness as predicted by diffusive ion transport. The molar fluxes observed for GO-P membranes in Table 4.1 are significantly higher than those observed in GO-PEG-L membranes and pristine GO. This can be attributed to PNIPAm experiencing less confinement in the GO membranes compared to PEG-L. Furthermore, since PNIPAm only contains one NH_2 group at its end chain, it doesn't cross-link adjacent GO sheets, remaining as a tethered chain and opening up the pore structure of the GO membrane. In Table 3.1, it was observed that the molar flux scales with the molecular weight of the polymer. The PNIPAm polymer used in this work has a molecular weight of 4 500 g/mol, which is between L3 (3 000 g/mol) and L6 (6 000 g/mol), yet the 1.0 mg GO-P membrane showed a molar flux similar to L20.

Table 4.1: Molar flux of $Ru(bpy)_3^{2+}$ through GO-P membranes of different mass

	Molar Flux (mmol/hr·m^2)		
GO-P mass (mg)	J_{25}	J_{45}	J_{45}/J_{25}
1.0	21.24	43.46	2.04
2.0	16.33	30.72	1.88
3.0	9.98	17.52	1.75
4.0	4.67	11.18	2.39

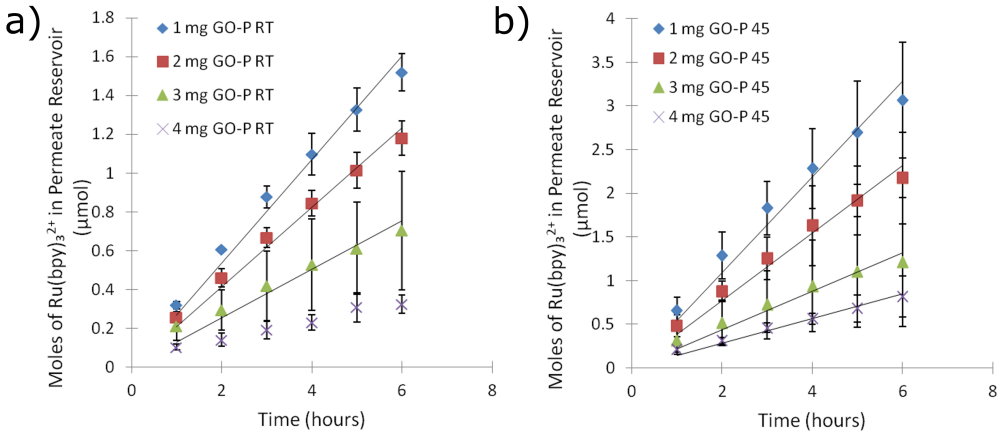

Figure 4.3: Permeation of $Ru(bpy)_3^{2+}$ through GO-P membranes. (a) Moles of $Ru(bpy)_3^{2+}$ transported from the feed to the permeate reservoir through GO-P membranes of various masses over 6 hours at 25 °C. (b) Moles of $Ru(bpy)_3^{2+}$ transported from the feed to the permeate reservoir through GO-P membranes of various masses over 6 hours at 45 °C. Error bars are ±1 standard deviation and the lines are linear fits.

For 1.0 - 4.0 mg GO-P membranes, the temperature ratio is greater than one, indicating that these membranes exhibit thermopositive responses when subjected to increases in temperature, which occur when diffusion is higher at T > LCST than T < LCST.[118,125] Furthermore, the diffusion coefficient can be written as a function of temperature, and the ratio of the diffusion coefficients at different temperatures can provide an insight to the source of the enhanced molar flux at elevated temperatures (see Appendix C). The evaluation of Equation C.2 using operating temperatures of 25 °C and 45 °C results in a diffusion coefficient ratio, D_{45}/D_{25}, equal to 1.599. This D ratio is equivalent to the theoretical ratio of J_{45}/J_{25}, as long as the ion and ion concentration gradients across the pores are the same. When comparing the temperature ratios obtained for the 1.0 - 4.0 mg membranes to the D ratio, it can be seen that the increased molar flux through the 1.0 - 4.0 mg GO-P membranes at elevated temperatures can be attributed mainly to the increase in the diffusion coefficient. This indicates that no phenomena relating to the abrupt structural change of PNIPAm at its LCST occurred. This could be due to two conditions. First, as mentioned at the beginning of this chapter, PNIPAm is a polymer whose stability and

structural change is highly sensitive to the surrounding water structure. It has been shown that the addition of salts to aqueous PNIPAm solutions reduce the LCST,[126–129] with the LCST decreasing with increasing salt concentrations. This is attributed to the Hofmeister series, which organizes cations and anions according to their ability to break or form water structures. The presence of ions disrupts the local water structure around the PNIPAm, causing a shift in the LCST. In this work, the ion concentration used is 20 mM (0.02 M), which indicates minimal or non-existent changes to the LCST occur (bulk LCST has been shown to decrease by 3-4 °C for a 0.25 M NaCl solution[127,128]). Secondly, the PNIPAm may not undergo the abrupt structural change due to the potential confinement imposed by the membrane structure, as both PNIPAm-grafted CNTs and PNIPAm-grafted GO in aqueous solution have shown LCST structural changes around 37 °C.[130,131]

It is important to investigate the behaviour of PNIPAm in GO-P membranes below the LCST and above the LCST in order to determine how the grafted PNIPAm behaves during ion permeation experiments. The scenarios for this behaviour are shown in Figure 4.4.

Below the LCST, PNIPAm molecules are hydrated with expanded configurations and the water around the polymers is immobile, resulting in low ion permeability.[122] Above the LCST, PNIPAm precipitates, sticking onto the surface of GO and water can pass through the open channels of the membrane (Figure 4.4a).[122] In this scenario, the effective interlayer spacing at 25 °C (d_{25}) would be lower than the effective interlayer spacing at 45 °C (d_{45}) as the coil-to-globular transition would increase the available space for ion permeation. If a coil-to-globular transition occurs, R_g scales from $aN^{3/5}$ to $aN^{1/3}$, where a is the size of the monomer and N is the degree of polymerization. If the polymer is confined in the interlayer spacing as discussed earlier, or covers the holes within GO sheets, voids formed between GO sheet edges, and/or large slits formed by folds/wrinkles, this would result in a significant increase in pore dimensions, drastically increasing the observed molar fluxes. Based on the results in Table 4.1, the scenario shown in Figure 4.4a is unlikely to occur as the enhancement at elevated temperatures can be explained by the increase in the diffusion coefficient.

However, depending on the grafting density and molecular weight of the PNIPAm, the

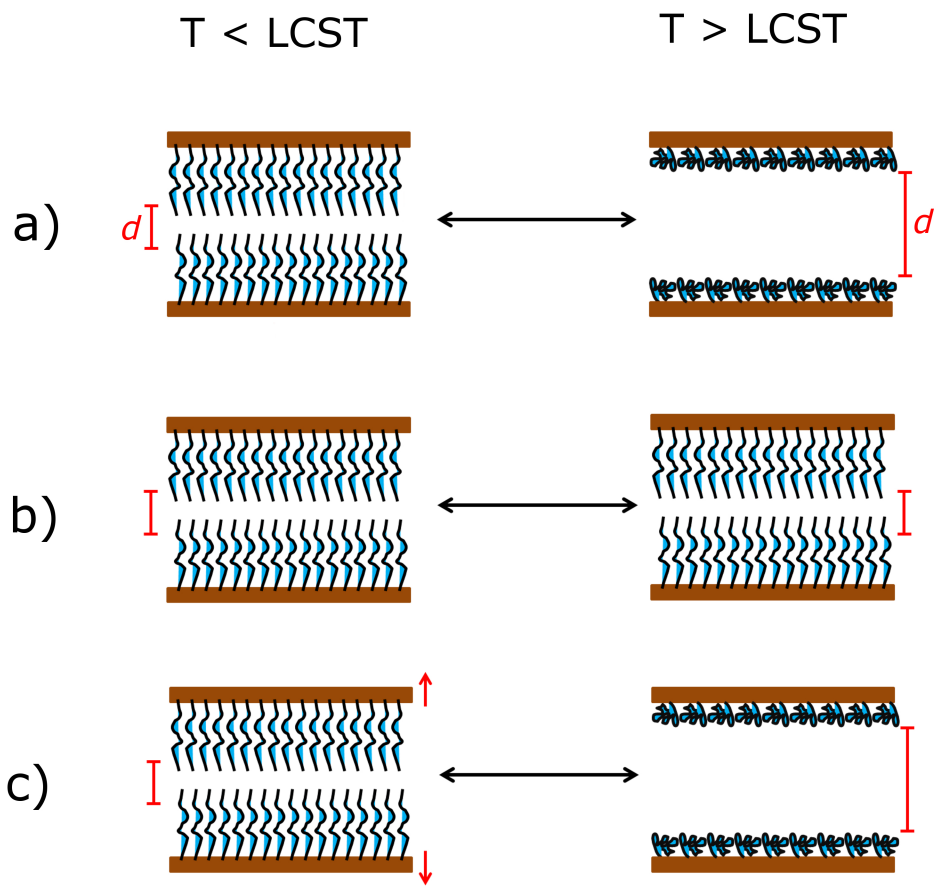

Figure 4.4: Schematic of different PNIPAm behaviours in GO-P membranes. (a) Coil-globular transition. (b) No transition or deformation. (c) Deformation due to swelling/deswelling of PNIPAm. The effective interlayer spacing is denoted as d.

quality of the LCST transition will be poor or non-existent,[132–134] resulting in $d_{25} = d_{45}$ (Figure 4.4b). It has been observed that regardless of molecular size of the solute, temperature has an opposite effect for those membranes with low grafting yields versus those of high grafting yields.[125] If the grafting yields are low, a solute is likely to undergo a thermopositive response due to the opening and closing of the pores from the swelling and shrinking of PNIPAm. If the grafting yield is high, diffusion is lower above LCST than it is below LCST (thermonegative response[118,125]) due to the hydrophobicity change in the PNIPAm. In addition, if grafting density is high, a polymer layer is formed over the pores, hindering diffusion.[122] For both GO-P and GO-PEG-L membranes, the potential grafting density is limited by the population and distance of carboxylic acid functional groups along the edges of the GO sheets as well as the conversion efficiency of the reaction.

It has been shown that low molecular weight and/or low grafting density PNIPAm does not collapse or have sharp changes in hydrophobic behaviour.[132–135] Since the molecular weight of PNIPAm used herein is only 4 500 g/mol, the J_{45}/J_{25} results in Table 4.1 match the D_{45}/D_{25} ratio (indicating no enhancement from PNIPAm), and the membranes undergo a thermopositive response, the GO-P membranes likely have low grafting yields and the scenario shown in Figure 4.4b strongly describes the behaviour of PNIPAm in GO-P membranes.

In addition, the swelling and shrinking of PNIPAM at the LCST can induce conformational changes in the substrate if the deformation force and pressure is stronger than the Van der Waals forces keeping the substrate together.[125] If this occurs, ion permeation would be significantly higher below the LCST since any swelling will deform and enlarge the porous structure of the membrane such that $d_{25} > d_{45}$ (Figure 4.4c). The molar fluxes recorded in Table 4.1 show that the 1.0 - 4.0 mg GO-P membranes had thermopositive responses at elevated temperatures, eliminating the scenario shown in Figure 4.4c.

As a result, by correlating the experimentally determined temperature ratio J_{45}/J_{25} with the theoretically calculated ratio of diffusion coefficients (D_{45}/D_{25}), it can be inferred that PNIPAm in GO-P membranes does not undergo a structural change above the LCST and the potential behaviour outlined in Figure 4.4b is the most likely occurring behaviour. This

may be due to the confinement imposed by the membrane structure and future work needs to be performed to explore these effects.

4.4 Conclusions

In summary, ion transport across functionalized GO membranes was investigated in order to optimize ion transport and to create stimuli-sensitive membranes by engineering the interlayer spacing of GO membranes. The addition of both PEG-L and PNIPAm altered the nanofluidic channel geometry, increasing the overall ion flux relative to pristine GO membranes.

Ion permeation was recorded through GO-P membranes for two different temperatures; T $<$ LCST and T $>$ LCST and observed molar fluxes were significantly higher than both GO-PEG-L and pristine GO membranes. This can be attributed to PNIPAm experiencing less confinement in the GO membranes compared to PEG-L. Furthermore, by correlating the experimentally determined temperature ratio J_{45}/J_{25} with the theoretically calculated ratio of diffusion coefficients (D_{45}/D_{25}) suggest that PNIPAm in GO-P membranes does not undergo a structural change above the LCST. This may be due to the confinement imposed by the membrane structure, and future work needs to be performed to explore these effects.

Chapter 5

Summary

Carbon nanomaterials such as carbon nanotubes and graphene have shown great promise as membranes due to their increased hydrodynamic and electrokinetic transport compared to conventional systems. CNTs have been fabricated into high density, alignable arrays with narrow pore distributions, while graphene has been fabricated with tunable thicknesses, surface areas and functionalities. The main goal of this work is to demonstrate the capabilities of carbon nanomaterials as potential next generation materials for membrane applications.

In Chapter 2, the ion transport across GO membranes of various thicknesses, made by vacuum filtration of GO aqueous solutions, were investigated in order to determine the effect of steric interactions on ion selectivity. The diffusive transport rates of two charge equivalent ruthenium complex ions $Ru(bpy)_3^{2+}$ and $Ru(phen)_3^{2+}$, with a sub-nanometer size difference, are distinguishable through relatively thick GO membranes (3 - 5 μm). Pore and slit-dominant hindered diffusion models for ion permeation through GO membranes were presented to characterize the transport through the nanochannels and nanopores within GO. Analysis of experimental results suggest that ion transport is mostly facilitated by large pores ($\geq$ 1.75 nm in diameter) in the relatively thin GO membranes, while slits formed by GO stacking ($\leq$1.42 nm in width) become dominant only in thick membranes. By grafting PEG molecules to the lateral plane of GO sheets, membranes with enlarged interlayer spacing were engineered, which showed drastically increased ion transport rates and lower distinction among the two ruthenium complex ions, consistent with the prediction by the slit-dominant steric hindered diffusion model.

In Chapter 3, ion transport across functionalized GO membranes was investigated in order to optimize ion transport and to create stimuli-sensitive membranes by engineering the

interlayer spacing of GO membranes. The addition PEG-L polymers of various molecular weight altered the nanofluidic channel geometry, increasing the overall ion flux relative to pristine GO membranes. The molar fluxes through PEGylated GO membranes were enhanced compared to pristine GO and scaled with molecular weight. The enhanced molar fluxes through PEGylated GO membranes was attributed to pore reconfigurations, ion-polymer, and ion-graphene interactions within the membrane. Analysis of J_{phen}/J_{bpy} ratios for the membranes determined that the shorter polymers tightened up and closed the larger pores, increasing the flux and selectivity while the longer polymers opened up the overall porous structure, increasing flux but not altering the observed selectivity.

In Chapter 4, GO was functionalized with an PNIPAm in order to design thermosensitive membranes. Ion permeation was recorded through GO-P membranes for two different temperatures; T $<$ LCST and T $>$ LCST and observed molar fluxes were significantly higher than both GO-PEG-L and pristine GO membranes. This can be attributed to PNIPAm experiencing less confinement in the GO membranes compared to PEG-L. Furthermore, by correlating the experimentally determined temperature ratio J_{45}/J_{25} with the theoretically calculated ratio of diffusion coefficients (D_{45}/D_{25}), PNIPAm in GO-P membranes does not undergo a structural change above the LCST. This was supported by evaluating the different transitions available for PNIPAm in the system.

Chapter 6

Future Work

Although ion transport was observed in both pristine and functionalized GO membranes, there are still many projects that need to be completed to demonstrate the capabilities of carbon nanomaterials as potential next generation materials for membrane applications.

First, it has been shown that graphene-based membranes are semi-permeable to solvents.[58] Furthermore, solvent selection has shown to increase the interlayer spacing of GO membranes.[136] The work herein has shown that manipulation of the pore structure influences permeation and selectivity characteristics of GO membranes. As a result to determine the self-diffusion coefficients of water and other solvents inside GO membranes, Pulse Gradient Spin Echo (PGSE) Proton Nuclear magnetic resonance (NMR) will be used. In this series of experiments, the diffusion of magnetization will be monitored and can occur in three general ways; spin-direction exchange between neighbouring nuclei due to dipole interactions, exchange-coupling via electrons, and by the self-diffusion of moment-bearing nuclei, the latter which will be the focus for this project.[137] The classical Bloch equation, which describes the macroscopic nuclear magnetization of a sample,[137] will be used in conjunction with the classical Stejskal-Tanner equation[138] in order to determine the values of the self-diffusion coefficients of H_2O and other solvents. Experiments for this project have been already been initiated; however, a combination of instrumentation concerns and parameter optimization have resulted in a temporary hiatus in the development of this work.

Second, conduct molecular dynamic simulations to investigate both polymer dynamics and ion transport in functionalized GO membranes. The results in Chapter 3 suggest that the enhancement over pristine GO is due to attributed to pore reconfigurations, ion-polymer, and ion-graphene interactions. Furthermore, the results in 4 suggest that the PNIPAm in GO-P membranes does not undergo a structural change above the LCST. This was

supported by evaluating the different transitions available for PNIPAm in the system, and the absence of any observed transition may be due to the confinement imposed by the membrane structure. Thus, simulations should be conducted using a graphene-based nanochannel utilizing a variety of grafting densities, polymers, and molecular weights in order to investigate and determine polymer characteristics in functionalized GO membranes.

Third, the knowledge of using electrokinetic methods such as electrophoresis or electro-osmosis with graphene-based systems is limited at this time. Many novel devices have been presented using CNTs; two-state Coulter counters,[32,33] ionic size-exclusion or surface-charge exclusion rectifying diodes,[37,38] and transdermal drug-delivery platforms.[139] Similar work using electrokinetic methods needs to be undertaken with graphene-based systems in order to determine the capabilities and applications of graphene-based membranes.

Fourth, the current experimental setup needs to be redesigned. The current experimental setup is convenient and easy to use, allowing for simultaneous data collection of diffusion. However, many commercial and industrial applications require the use of pressure-driven flow. In order to conduct pressure-driven experiments, the current experimental setup will require changing. This can be achieved in two ways; altering the macroscopic size and shape of the GO membranes to fit into conventional membrane instruments, or redesigning the experimental setup in order to integrate pressure-driven equipment into the device.

Finally, process capability studies need to be undertaken in order to standardize GO formulation and membrane fabrication. This will decrease variability in membrane thickness (for a given GO mass) as membrane thickness vary reported molar fluxes. This project will involve two or more operators performing the entire life-cycle of the GO formulation and experimental setup procedure simultaneously, measuring the variation of key attributes such as C/O ratio, GO concentration, membrane thickness (for a given GO mass) effect of vacuum pressure on membrane structure and thickness, and standardizing the process to minimize any major deviations.

APPENDICES

Appendix A

Absorbance Spectra

A.1 Concentration Standards of $Ru(bpy)_3^{2+}$ and $Ru(phen)_3^{2+}$ in Aqueous Solution

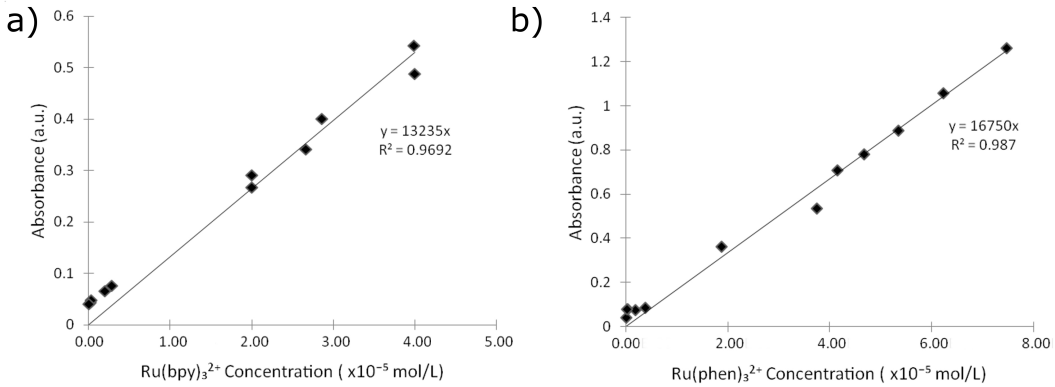

Figure A.1: (a) Concentration standard curve at 450 nm for the $Ru(bpy)_3^{2+}$ complex in aqueous solution at room temperature. (b) Concentration standard curve at 448 nm for the $Ru(phen)_3^{2+}$ complex in aqueous solution at room temperature.

Figure A.1a shows the magnitude of the absorbance peak at $\lambda = 450$ nm for the $Ru(bpy)_3^{2+}$ complex in aqueous solution at room temperature for a variety of concentrations. Similarly, Figure A.1b shows the magnitude of the absorbance peak at $\lambda = 448$ nm for the $Ru(phen)_3^{2+}$ complex in aqueous solution at room temperature for a variety of concentrations. The absorbance peaks at $\lambda = 450 \pm 2$ nm for $Ru(bpy)_3^{2+}$ and 447 ± 2 nm for $Ru(phen)_3^{2+}$ are associated with a metal to ligand charge transfer (MLCT) between the ruthenium metal and the 2,2-bipyridine (or 1,10-phenanthroline) ligand.[140] By applying linear regression to

the data points in Figure A.1a, the molar extinction coefficient of $Ru(bpy)_3^{2+}$ used in this work was 13 235 L M^{-1} cm^{-1}, a 9.3 % error from the theoretical value of 14 600 L M^{-1} cm^{-1}.[140] Similar analysis to the data points in Figure A.1b resulted in a molar extinction coefficient of 16 750 for the $Ru(phen)_3^{2+}$ complex, an error of 11.8% compared to the theoretical value of 19 000 L M^{-1} cm^{-1}.[140]

A.2 Absorbance Spectra of $Ru(bpy)_3^{2+}$ and $Ru(phen)_3^{2+}$ in Permeate Reservoir

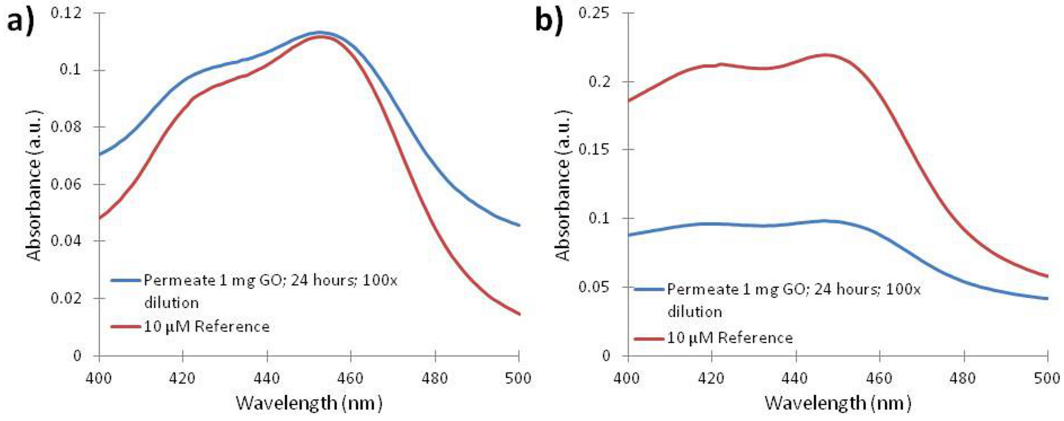

Figure A.2: (a) Adsorption spectra for the $Ru(bpy)_3^{2+}$ complex in aqueous solution at room temperature for a 100 times dilution of a 1 mg GO film permeate reservoir after 24 hours. (b) Adsorption spectra for the $Ru(phen)_3^{2+}$ complex in aqueous solution at room temperature for a 100 times dilution of a 1 mg GO film permeate reservoir after 24 hours.

Figure A.2a shows the absorption spectrum of a 100x dilution of a 1 mg GO film permeate reservoir after 24 hours for the $Ru(bpy)_3^{2+}$ complex in aqueous solution at room temperature. Similarly, Figure A.2b shows the absorption spectrum of a 100x dilution of a 1 mg GO film permeate reservoir after 24 hours for the $Ru(phen)_3^{2+}$ complex in aqueous solution at room temperature. The overlaps of peak location between permeate and reference spectra in Figure A.2 indicate that the metal complex remains intact throughout

the experiment and no decomposition occurs when interacting with the GO films. The magnitude difference between the two complexes for the same reference concentration is due to the variance in the molar extinction coefficient between the two ions.

A.3 Effect of Temperature on the Molar Extinction Coefficient

In order to determine the effects of temperature on the molar extinction coefficient of $Ru(bpy)_3^{2+}$ during elevated mass transport experiments, a 20 mL 0.1 mM $Ru(bpy)_3^{2+}$ standard was placed in the oven with the GO-P membranes and 1 mL aliquots of solution were sampled along with the GO-P membranes at various time points over 6 hours. Figure A.3 shows the average percentage decrease of the absorbance over the duration of the experiment.

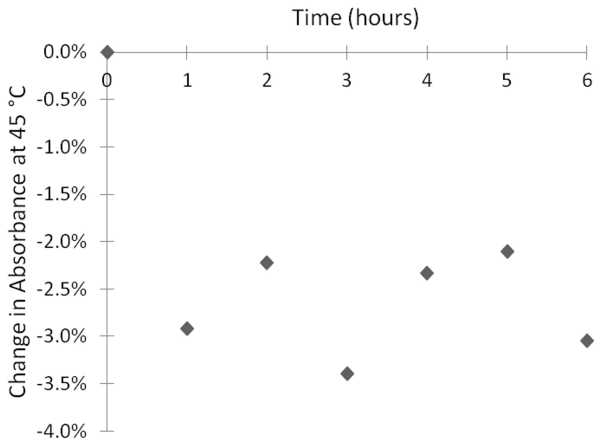

Figure A.3: Effect of temperature on the $Ru(bpy)_3^{2+}$ molar extinction coefficient

Appendix B

Characterization of Functionalized GO Membranes

B.1 PEGylated GO (GO-PEG-L#)

B.1.1 FTIR

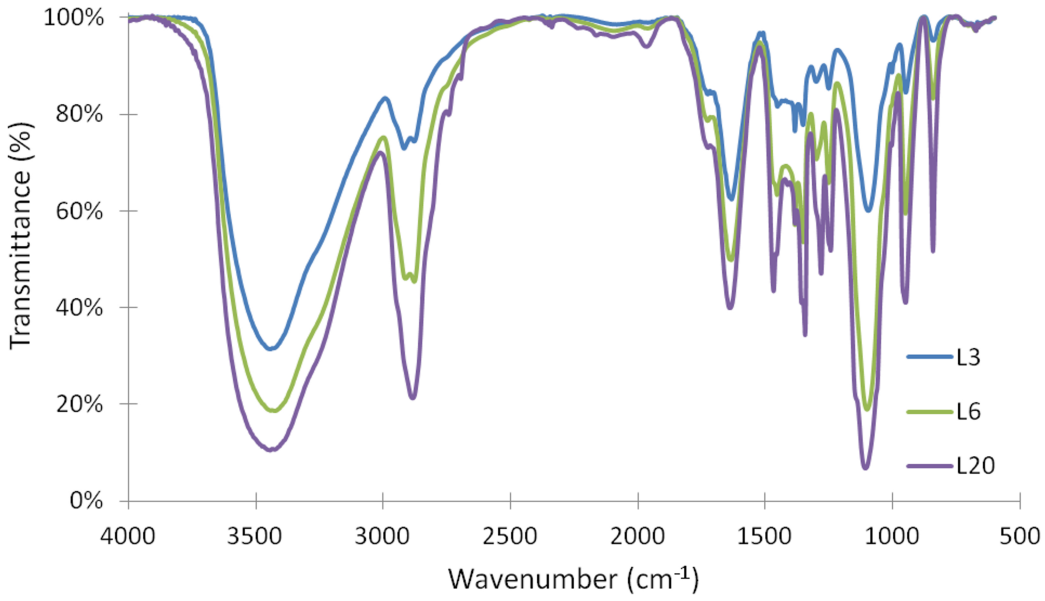

Figure B.1: FTIR spectra of GO-PEG-L3, L6, and L20 membranes.

B.1.2 TGA

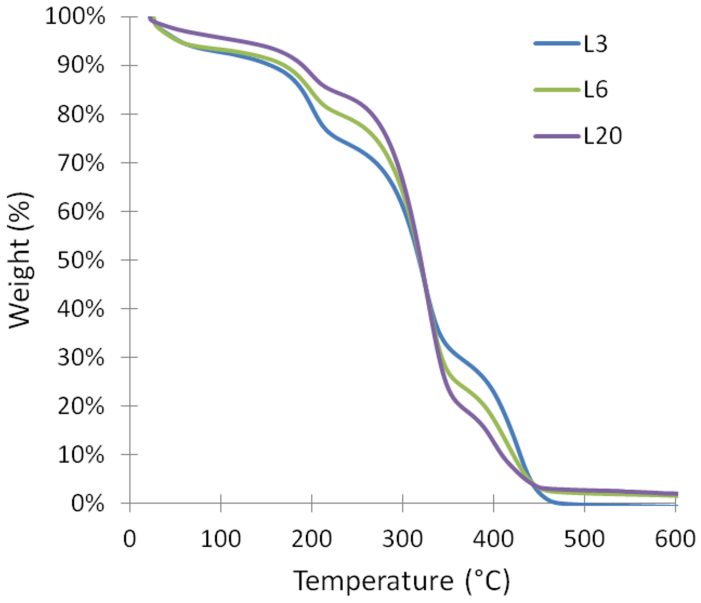

Figure B.2: TGA of GO-PEG-L3, L6, and L20 membranes.

B.2 GO-PNIPAm (GO-P)

B.2.1 XRD

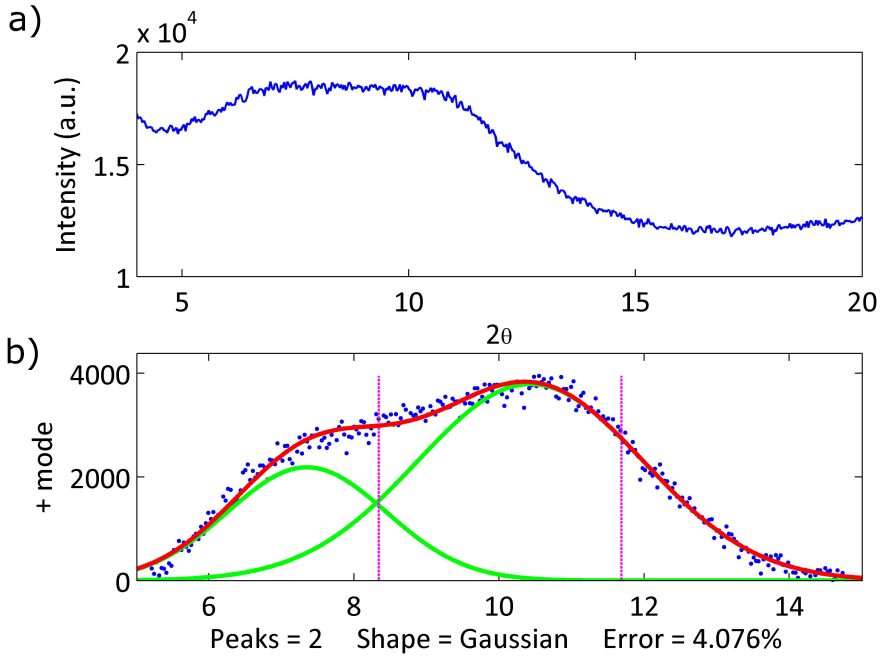

Figure B.3: GO-P membrane characteristics. (a) XRD spectra of GO-P1 membrane with the interlayer diffraction peak identified. (b) Deconvolution of interlayer diffraction peak using *Peak Fitter Version 5.5* MATLAB program[124] including peak location, residuals, and root-mean-square error of the best fit.

Table B.1: XRD Peak Positions and Interlayer Spacing of GO-PNIPAm

Sample	Peak Location 2θ (°)	Interlayer Spacing d (nm)	Error† (%)
GO-P	7.36	1.20	4.07[2]
	10.02	0.88	

†n^{th}-order baseline correction that minimizes root-mean-square error; 1 = linear; 2 = quadratic

B.3 Determining Polymer Properties in Aqueous Solution

The following MATLAB scripts were compiled to calculate the properties of PEG-L [104,109,111,141–144] and PNIPAm [104,116,144–147] in aqueous solution.

B.3.1 PEG-L

```
%Determining various properties of PEG-L @ T = 298.15K
%%
%References
%[1] Keinberger, F.; Pastushenko, V.P.; Kada, G.; Gruber, H.J.; Riener, C.;
    %Schindler, H.; Hinterdorfer, P. Single Molecules 2000, 1, 123-128
%[2] Oesterhelt, F.; Rief, M.; Gaub, H.E. New Journal of Physics 1999, 1,
    %6.1-6.11
%[3] Bhat, R.; Timasheff, S.N. Protein Science 1992, 1, 1133-1143.
%[4] Devanand, K.; Selser, J.C. Macromolecules 1991, 24, 5943-5947
%[5] Holyst, R.; Bielejewska, A.; Szymanski, J.; Wilk, A.; Patkowski, A.;
    %Gapinski, J.; Zywocinshi, A.; Kalwarczyk, T.; Kalwarczyk, E.; Tabaka, M.;
    %Ziebacz, N.; Wieczorek, S. Physical Chemistry Chemical Physics 2009, 11,
    %9025-9032.
%[6] Ollila, S.T.T.; Denniston, C.; Karttunen, M.; Ala-Nissila, T.
    %Hydrodynamic effects on confined polymers. Soft Matter 2013, 9,
    %3478-3487
%[7] Linegar, K.L.; Adeniran, A.E.; Kostko, A.F.; Anisimov, M.A.
    %Colloid Journal 2010, 72, 279  2 8 1
%%
%Parameters
Mn = input('Input Mn (or Mw) of Polymer (g/mol) - (in a nx1 matrix):');
Mo = (44.0526); %Monomer Molecular Weight (CH2CH2O) (g/mol)
Me = (60.0983);  %End Group Molecular Weight        (g/mol)
N = (Mn - Me)./Mo; %Number of Monomers              (unitless)
NA = 6.023e23; %Avogadro's Number                   (1/mol)
lp = 0.38;  %Persistence Length                     (nm)            [1]
```

```
lk = 0.7;   %Kuhn Length                                (nm)            [2]
a = 0.278;  %Length of individual PEG unit              (nm)            [2,3]
T = 298.15; %Temperature                                (K)
rho = 1.128; %Density                                   (g/cm3)
k = 1.38064e-23; %Boltzmann Constant                    (J/K)
Rp = 0.633; %Ru(bpy)3^2+ radius                         (nm)
dz = 1.13; %Interlayer spacing determined by XRD        (nm)
%%
%Polymer Properties in Aqueous Solution
A = 1.84e-2.*Mn.^(-1/4) %2nd Virial Coefficient         (cm3 mol/g^-2)  [4]
Rg = 0.0215.*Mn.^(0.583) %Radius of Gyration            (nm)            [3-5]
parRg = sqrt(2/3).*Rg; % Parallel Component of Rg       (nm)            [6]
Rh = 0.0145.*Mn.^(0.571) %Hydrodynamic Radius           (nm)            [3-5,7]
Rgh = Rg/Rh   %Ratio of Radii                           (unitless)
Cstar = Mn./((4/3).*pi.*Rg.^3.*NA)./1e-21 %Overlap Concentration (g/cm3)[5]
Climit = Cstar.*(Rp./Rg).^(4./3) %(g/cm3) Above this limit probe
                                 %(i.e. Ru(bpy)3^2+) should experience
                                 %macroscopic solution viscosity [5]
%%
%Polymer Properties under confinement
Cf = Rg./dz                 %If 1 < Cf << Rg./lp = de Gennes regime  [6]
DGlimit = Rg./lp
DG = Cf;                  %Determine if in de Gennes regime
for i = 1:length(Cf)
    if DG(1,i)< DGlimit(1,i)
    DG(1,:) = 1;
    else DG(1,:) = 0;
        i=i+1;
    end
end
disp(DG)
invCf = 1./Cf
parRCf = Rg.*Cf.^(0.25)
```

B.3.2 PNIPAm

```
%Determining various properties of PNIPAm @ T = 25C
%%
%References
%[1]Zhang, W.; Zou, S.; Wang, C.; Zhang, X. Journal of Physical Chemistry B
   %2000, 104, 10258-10264
%[2]Kubota, K.; Hamano, K.; Kuwahara, N.; Fujishige, S.; Ando, I.
   %Polymer Journal 1990, 22, 1051-1057
%[3]Zhu, X.; Yan, C.; Winnick, F.M.; Leckband, D. Langmuir 2007, 23,
%   162-169
%[4]Kubota, K.; Fujishige, S.; Ando, I. Polymer Journal 1990, 22, 15-20
%[5]Ke, X.-X.; Wang, L.; Xu, J.-T,; Du, B.-Y.; Tu, Y.-F.; Fan, Z.-Q. Soft
   %Matter 2014, 10, 5201-5211
%[6] Holyst, R.; Bielejewska, A.; Szymanski, J.; Wilk, A.; Patkowski, A.;
    %Gapinski, J.; Zywocinshi, A.; Kalwarczyk, T.; Kalwarczyk, E.; Tabaka, M.;
    %Ziebacz, N.; Wieczorek, S. Physical Chemistry Chemical Physics 2009, 11,
    %9025-9032
%[7] Ollila, S.T.T.; Denniston, C.; Karttunen, M.; Ala-Nissila, T.
    %Hydrodynamic effects on confined polymers. Soft Matter 2013, 9,
    %3478-3487
%[8]Bittrich, E.; Burkert, S.; Muller, M.; Eichhorn, K.-J.; Stamm, M.;
   %Uhlmann, P. Temperature-Sensitive Swelling of Poly(N-isopropylacrylamide)
   %brushes %with low Molecular Weight and Grafting Density.
   %Langmuir 2012, 28, 3439-3448
%[9]Milner, S.T. Science 1991, 251, 905-914
%%
%Parameters
Mn = input('Input Mn of Polymer (g/mol):');%Molecular Weight of Polymer
Mo = 113.1576; %Monomer Molecular Weight            (g/mol)
Me = 76.1407; %End Group Molecular Weight           (g/mol)
N = (Mn - Me)/Mo; %Number of Monomers               (unitless)
NA = 6.023e23;    %Avogadro's Number                (1/mol)
lp = 0.38;  %Persistence Length                     (nm)
lk = 0.68;  %Kuhn Length                            (nm)            [1]
a = 0.25;   %Length of individual PNIPAm unit       (nm)            [2,3]
```

```
T = 298.15; %Temperature                                    (K)
rho = 1.07; %Density                                        (g/cm3)
k = 1.38064e-23;  %Boltzmann Constant                       (J/K)
Rp = 0.633; %Ru(bpy)3^2+ radius                             (nm)
dz = 1.13; %Interlayer spacing determined by XRD            (nm)
%%
%Polymer Properties in Aqueous Solution
A = 5.9e-3*Mn^(-1/4);  %2nd Virial Coefficient              (cm3 mol/g^-2)    [2]
Rg = 0.0224*Mn^(0.54) %Radius of Gyration                   (nm)              [4]
Rh = 0.0160*Mn^(0.54); %Hydrodynamic Radius                     (nm)          [4]
Rgh = Rg/Rh    %Ratio of Radii                              (unitless)
RF = a*N^(3/5)  %Flory Radius
%eta = 0.112*Mn^(-0.51)  %Intrinsic Viscosity               (cm3/g)           [4]
%Psi = (A*Mn^2)/(4*pi^(3/2)*NA*(Rg*1e-7)^3) %Interpenetration Function
                                                            %(unitless)       [4]
%exV = 2*9A*Mo^2/((a*1e-7)^3*NA) %Excluded Volumer Parameter
                                                            %(unitless)       [5]
Cstar = Mn./((4/3).*pi.*Rg.^3.*NA)./1e-21 %Overlap Concentration (g/cm3)[6]
Climit = Cstar.*(Rp./Rg).^(4./3) %(g/cm3) Above this limit probe
                                 %(i.e. Ru(bpy)3^2+) should experience
                                 %macroscopic solution viscosity [6]
%%
%Polymer Properties under confinement
Cf = Rg./dz                %If 1 < Cf << Rg./lp = de Gennes regime   [7]
DGlimit = Rg./lp
DG = Cf;                  %Determine if in de Gennes regime
for i = 1:length(Cf)
    if DG(1,i)< DGlimit(1,i)
    DG(1,:) = 1;
    else DG(1,:) = 0;
        i=i+1;
    end
end
disp(DG)
invCf = 1./Cf
parRCf = Rg.*Cf.^(0.25)
```

Appendix C

Effect of Temperature on Diffusion

Using the Stokes-Einstein equation, the relationship between the diffusion coefficient and temperature can be obtained,

$$D_{T_i} = \frac{k_B T_i}{6\pi\eta R_s} \tag{C.1}$$

$$\frac{D_{T_i}\eta_i}{T_i} = constant \tag{C.2}$$

where D_{T_i} is the bulk diffusivity at temperature i, k_B is the Boltzmann constant, η is the viscosity of the liquid at temperature i, T_i is the temperature (in Kelvin), and R_s is the hydrodynamic radius of the solute molecule. For mass transport experiments performed at elevated temperatures, the effect of temperature on the diffusion coefficient can be obtained by taking the ratio of Equation C.2.

$$\frac{D_{T_i}}{D_{T_j}} = \frac{\eta_j T_i}{\eta_i T_j} \tag{C.3}$$

In this work, mass transport experiments are conducted at 45 °C, so the ratio becomes the following,

$$\frac{D_{45}}{D_{25}} = 1.59914 \tag{C.4}$$

References

[1] Lakshminarayanaiah, N. *Chemical Reviews* **1965**, *65*, 491–565.

[2] Daufin, G.; Escudier, J.-P.; Carrère, H.; Bérot, L., S. Fillaudeau; Decloux, M. *Food and Bioproducts Processing* **2001**, *79*, 89–102.

[3] Girard, B.; Fukumoto, L.; Koseoglu, S. *Critical Reviews in Biotechnology* **2000**, *20*, 109–175.

[4] Heath, C.; Belfort, G. In *Advances in Biochemical Engineering/Biotechnology Vol. 47*; Fiechter, A., Ed.; Springer-Verlag, 1992; pp 45–86.

[5] Sridhar, S.; Smitha, B.; Aminabhavi, T. *Separation and Purifaction Reviews* **2007**, *36*, 113–174.

[6] Peighambardoust, S.; Rowshanzamir, S.; Amjadi, M. *International Journal of Hydrogen Energy* **2010**, *35*, 9349–9384.

[7] Jarusutthirak, C.; Amy, G.; Croue, J. *Desalination* **2002**, *145*, 247–255.

[8] Snyder, S.; Adham, S.; Redding, A.; Cannon, F.; DeCarolis, J.; Oppenheimer, J.; Wert, E.; Yoon, Y. *Desalination* **2007**, *202*, 156–181.

[9] Hilal, N.; Al-Zoubi, H.; Darwish, N.; Mohammad, A.; Abu Arabi, M. *Desalination* **2004**, *170*, 281–308.

[10] Shannon, M.; Bohn, P.; Elimelech, M.; Georgiadis, J.; Marinas, B.; Mayes, A. *Nature* **2008**, *452*, 301–310.

[11] Greenlee, L.; Lawler, D.; Freeman, B.; Marrot, B.; Moulin, P. *Water Research* **2019**, *43*, 2317–2348.

[12] Becker, W.; Kleinsmith, L.; Hardin, J.; Bertoni, G. *The World of the Cell*, 7th ed.; Pearson/Benjamin Cummings, 2009; pp 196–211.

[13] Deen, W. *American Institute of Chemical Engineers Journal* **1987**, *33*, 1409–1425.

[14] Dechadilok, P.; Deen, W. *Industrial and Engineering Chemical Research* **2006**, *45*, 6953–6959.

[15] Chun, M.-S.; Phillips, R. *American Institute of Chemical Engineers Journal* **1997**, *43*, 1194–1203.

[16] Dechadilok, P.; Deen, W. *Journal of Membrane Science* **2009**, *336*, 7–16.

[17] Chen, S. *Journal of Colloid and Interface Science* **1998**, *205*, 354–364.

[18] Bungay, P.; Brenner, H. *International Journal of Multiphase Flow* **1973**, *1*, 25–56.

[19] Schoch, R.; Han, J.; Renaud, P. *Reviews of Modern Physics* **2008**, *80*, 839–883.

[20] Hummer, G.; Rasaiah, J.; Noworyta, J. *Nature* **2001**, *414*, 188–190.

[21] Kalra, A.; Garde, S.; Hummer, G. *Proceedings of the National Academy of Sciences of the United States of America* **2003**, *100*, 10175–10180.

[22] Sokhan, V.; Nicholson, D.; Quirke, N. *Journal of Chemical Physics* **2002**, *117*, 8531–8539.

[23] Joseph, S.; Aluru, N. *Nano Letters* **2008**, *8*, 452–458.

[24] Majumder, M.; Chopra, N.; Hinds, B. *ACS Nano* **2011**, *5*, 3867–3877.

[25] Hinds, B.; Chopra, N.; Rantell, T.; Andrews, R.; Gavalas, V.; Bachas, L. *Science* **2004**, *303*, 62–65.

[26] Majumder, M.; Chopra, N.; Hinds, B. *Journal of the American Chemical Society* **2005**, *127*, 9062–9070.

[27] Hinds, B. *Current Opinion in Solid State and Material Science* **2012**, *16*, 1–9.

[28] Wu, J.; Gerstandt, K.; Majumder, M.; Zhan, X.; Hinds, B. *Nanoscale* **2011**, *3*, 3321–3328.

[29] Holt, J.; Park, H.; Wang, Y.; Stadermann, M.; Artyukhin, A.; Grigoropoulos, C.; Noy, A.; Bakajin, O. *Science* **2006**, *312*, 1034–1037.

[30] Majumder, M.; Chopra, N.; Andrews, R.; Hinds, B. *Nature* **2005**, *438*, 44.

[31] Miller, S.; Young, V.; Martin, C. *Journal of the American Chemical Society* **2001**, *123*, 12335–12342.

[32] Lee, C.; Choi, W.; Han, J.-H.; Strano, M. *Science* **2010**, *329*, 1320–1324.

[33] Choi, W.; Ulissi, Z.; Shimizu, S.; Bellisario, D.; Ellison, M.; Strano, M. *Nature Communications* **2013**, *4*, doi:10.1038/ncomms3397.

[34] Clarke, J.; Wu, H.-C.; Jayasinghe, L.; Patel, A.; Reid, S.; Bayley, H. *Nature Nanotechnology* **2009**, *4*, 265–270.

[35] Rotem, D.; Jayasinghe, L.; Salichou, M.; Bayley, H. *Journal of the American Chemical Society* **2012**, *134*, 2781–2787.

[36] Bayley, H.; Cremer, P. *Nature* **2001**, *413*, 226–230.

[37] Wu, J.; Gerstandt, K.; Zhang, H.; Liu, J.; Hinds, B. *Nature Nanotechnology* **2012**, *7*, 133–139.

[38] Scruggs, N.; Robertson, J.; Kasianowicz, J.; Migler, K. *Nano Letters* **2009**, *9*, 3853–3859.

[39] Vlassiouk, I.; Smirnov, S.; Siwy, Z. *Nano Letters* **2008**, *8*, 1978–1985.

[40] Wells, D.; Belkin, M.; Comer, J.; Aksimentiev, A. *Nano Letters* **2012**, *12*, 4117–4123.

[41] Sint, K.; Wang, B.; Král, P. *Journal of the American Chemical Society* **2008**, *130*, 16448–16449.

[42] Suk, M.; Aluru, N. *Journal of Physical Chemistry Letters* **2010**, *1*, 1590–1594.

[43] Hu, G.; Mao, M.; Ghosal, S. *Nanotechnology* **2012**, *23*, 395501.

[44] O'Hern, S.; Stewart, C.; Boutilier, M.; Idrobo, J.-C.; Bhaviripudi, S.; Das, S.; Kong, J.; Laoui, T.; Atieh, M.; Karnik, R. *ACS Nano* **2012**, *6*, 10130–10138.

[45] Cohen-Tanugi, D.; Grossman, J. *Nano Letters* **2012**, *12*, 3602–3608.

[46] O'Hern, S.; Boutilier, M.; Idrobo, J.-C.; Song, Y.; Kong, J.; Laoui, T.; Atieh, M.; Karnik, R. *Nano Letters* **2014**, *14*, 1234–1241.

[47] Lerf, A.; He, H.; Forster, M.; Klinowski, J. *Journal of Physical Chemistry B* **1998**, *102*, 4477–4482.

[48] Gómez-Navarro, C.; Meyer, J.; Sundaram, R.; Chuvilin, A.; Kurasch, S.; Burghard, M.; Kern, K.; Kaiser, U. *Nano Letters* **2010**, *10*, 1144–1148.

[49] Erickson, K.; Erni, R.; Lee, Z.; Alem, N.; Gannett, W.; Zettl, A. *Advanced Materials* **2010**, *22*, 4467–4472.

[50] Hu, M.; Mi, B. *Environmental Science & Technology* **2013**, *47*, 3715–3723.

[51] Sun, P.; Zhu, M.; Wang, K.; Zhong, M.; Wei, J.; Wu, D.; Xu, Z.; Zhu, H. *ACS Nano* **2013**, *7*, 428–437.

[52] Joshi, R.; Carbone, P.; Wang, F.; Kravets, V.; Su, Y.; Grigorieva, I.; Wu, H.; Geim, A.; Nair, R. *Science* **2014**, *343*, 752–754.

[53] Raidongia, K.; Huang, J. *Journal of the American Chemical Society* **2012**, *134*, 16528–16531.

[54] Huang, H.; Mao, Y.; Liu, Y.; Sun, L.; Peng, X. *Chemical Communications* **2013**, *49*, 5963–5965.

[55] Han, Y.; Xu, Z.; Gao, C. *Advanced Functional Materials* **2013**, *23*, 3693–3700.

[56] Georgakilas, V.; Otyepka, M.; Bourlinos, A.; Chandra, V.; Kim, N.; Kemp, K.; Hobza, P.; Zboril, R.; Kim, K. *Chemical Reviews* **2012**, *112*, 6156–6214.

[57] Willliams, A.; Ibrahim, I. *Chemical Reviews* **1981**, *81*, 589–636.

[58] Nair, R.; Wu, H.; Jayaram, P.; Grigorieva, I.; Geim, A. *Science* **2012**, *335*, 442–44.

[59] Choi, W.; Choi, J.; Bang, J.; Lee, J.-H. *ACS Applied Materials and Interfaces* **2013**, *5*, 1250–12519.

[60] Boukhvalov, D.; Katsnelson, M.; Son, Y.-W. *Nano Letters* **2013**, *13*, 3930–3935.

[61] Wei, N.; Peng, X.; Xu, Z. *Physical Review E* **2014**, *89*, 012113.

[62] Wei, N.; Lv, C.; Xu, Z. *Langmuir* **2014**, *30*, 3572–3578.

[63] Wei, N.; Peng, X.; Xu, Z. *ACS Applied Materials and Interfaces* **2014**, *6*, 5877–5883.

[64] Guo, W.; Cheng, C.; Wu, Y.; Jiang, Y.; Gao, J.; Li, D.; Jiang, L. *Advanced Materials* **2013**, *25*, 6064–6068.

[65] Sun, P.; Zheng, F.; Zhu, M.; Song, Z.; Wang, K.; Zhong, M.; Wu, D.; Little, R.; Zhu, H. *ACS Nano* **2014**, *8*, 850–859.

[66] Sun, P.; Zheng, F.; Zhu, M.; Wang, K.; Zhong, M.; Wu, D.; Zhu, H. *Scientific Reports* **2014**, *4*, 80–87.

[67] Choi, J.; Alexandrova, M.; Par, H. In *Carbon Nanotubes Applications on Electronic Devices*; Marulanda, J., Ed.; InTech, 2011; pp 405–454.

[68] Nednoor, P.; Gavalas, V.; Chopra, N.; Hinds, B.; Bachas, L. *Journal of Materials Chemistry* **2007**, *17*, 1755–1757.

[69] Beu, T. *Journal of Chemical Physics* **2011**, *135*, 044515.

[70] Song, C.; Corry, B. *Journal of Physical Chemistry B* **2009**, *113*, 7642–7649.

[71] Zwolak, M.; Wilson, J.; Di Ventra, M. *Journal of Physics: Condensed Matter* **2010**, *22*, 454126.

[72] Beu, T. *Journal of Chemical Physics* **2011**, *135*, 044516.

[73] Dzubiella, J.; Hansen, J. *Journal of Chemical Physics* **2005**, *122*, 234706.

[74] Beu, T. *Journal of Chemical Physics* **2010**, *132*, 164513.

[75] Xu, Y.; Aluru, N. *Applied Physics Letters* **2008**, *93*, 043122.

[76] Nednoor, P.; Chopra, N.; Gavalas, V.; Bachas, L.; Hinds, B. *Chemistry of Materials* **2005**, *17*, 3595–3599.

[77] Huang, H.; Song, Z.; Wei, N.; Shi, L.; Mao, Y.; Ying, Y.; Sun, L.; Xu, Z.; Peng, X. *Nature Communications* **2013**, *4*, 2979:doi:10.1038/ncomms3979.

[78] Mi, B. *Science* **2014**, *343*, 740–742.

[79] Maloney, D.; MacDonnell, F. *Acta Crystallographica Section C* **1997**, *C53*, 705–707.

[80] Rillema, D.; Jones, D. *Journal of the Chemical Society, Chemical Communications* **1979**, *19*, 849–851.

[81] Moret, M.-E.; Tavernelli, I.; Rothlisberger, U. *Journal of Physical Chemistry B* **2009**, *113*, 7737–7744.

[82] Szymczak, J.; Hofmann, F.; Meuwly, M. *Physical Chemistry Chemical Physics* **2013**, *15*, 6268–6277.

[83] Hummers, W.; Offeman, R. *Journal of the American Chemical Society* **1958**, *80*, 1339–1339.

[84] Kovtyukhova, N.; Ollivier, P.; Martin, B.; Mallouk, T.; Chizhik, S.; Buzaneva, E.; Gorchinskiy, A. *Chemistry of Materials* **1999**, *11*, 771–778.

[85] Gao, X.; Tang, S. *Carbon* **2014**, *76*, 133–140.

[86] Coleman, M.; Tang, S. *Nano Research* **2014**, DOI 10.1007/s12274–014–0593–x.

[87] Wilke, C.; Chang, P. *American Institute of Chemical Engineers Journal* **1955**, *1*, 264–270.

[88] Martin, C.; Rubinstein, I.; Bard, A. *Journal of Electroanalytical Chemistry* **1983**, *151*, 267–271.

[89] Boutilier, M.; Sun, C.; OHern, S.; Au, H.; Hadjiconstantinou, N.; Karnik, R. *ACS Nano* **2014**, *8*, 841–849.

[90] Silva, V.; Pradanos, P.; Palacio, L.; Hernandez, A. *Desalination* **2009**, *245*, 606–613.

[91] Kuila, T.; Bose, S.; Mishra, A.; Khanra, P.; Kim, N.; Lee, J. *Progress in Materials Science* **2012**, *57*, 1061–1105.

[92] Bourlinos, A.; Gournis, D.; Petridis, D.; Szabo, T.; Szeri, A.; Dekany, I. *Langmuir* **2003**, *19*, 6050–6055.

[93] Liu, Z.; Robinson, J.; Sun, X.; Dai, H. *Journal of the American Chemical Society* **2008**, *130*, 10876–10877.

[94] Mallakpour, S.; Abdolmaleki, A.; Borandeh, S. *Applied Surface Science* **2014**, *307*, 533–542.

[95] Tasis, D.; Tagmatarchis, N.; Bianco, A.; Prato, M. *Chemical Reviews* **2006**, *106*, 1105–1136.

[96] Bahr, J.; Yang, J.; Kosynkin, D.; Bronikowski, M.; Smalley, R.; Tour, J. *Journal of the American Chemical Society* **2001**, *123*, 6536–6542.

[97] Wu, J.; Zhan, X.; Hinds, B. *Chemical Communications* **2012**, *48*, 7979–7981.

[98] Hu, M.; Mi, B. *Journal of Membrane Science* **2014**, *469*, 80–87.

[99] Wang, C.; Feng, L.; Yang, H.; Xin, G.; Li, W.; Zheng, J.; Tian, W.; Li, X. *Physical Chemistry Chemical Physics* **2012**, *14*, 13233–13238.

[100] Brochard, F. *Journal de Physique* **1977**, *38*, 1285–1291.

[101] Brochard, F.; de Gennes, P. *Journal of Chemical Physics* **1977**, *67*, 52–56.

[102] Odijk, T. *Macromolecules* **1983**, *16*, 1340–1344.

[103] Dai, L.; Jones, J.; van der Maarel, J.; Doyle, P. *Soft Matter* **2012**, *8*, 2972–2982.

[104] Ollila, S.; Denniston, C.; Karttunen, M.; Ala-Nissila, T. *Soft Matter* **2013**, *9*, 3478–3487.

[105] Tang, J.; Levy, S.; Trahan, D.; Jones, J.; Craighead, H.; Doyle, P. *Macromolecules* **2010**, *43*, 7368–7377.

[106] Bonthuis, D.; Meyer, C.; Stein, D.; Dekker, C. *Physical Review Letters* **2008**, *101*, 108303.

[107] Chen, Y.-L.; Graham, M.; de Pablo, J.; Randall, G.; Gupta, M.; Doyle, P. *Physical Review E* **2004**, *70*, 060901.

[108] Hsu, H.-P.; Grassberger, P. *Journal of Chemical Physics* **2004**, *120*, 2034–2041.

[109] Keinberger, F.; Pastushenko, V.; Kada, G.; Gruber, H.; Riener, C.; Schindler, H.; Hinterdorfer, P. *Single Molecules* **2000**, *1*, 123–128.

[110] Oelmeier, S.; Dismer, F.; Hubbuch, J. *BMC Biophysics* **2012**, *5*, 14–28.

[111] Devanand, K.; Selser, J. *Macromolecules* **1991**, *24*, 5943–5947.

[112] Koenig, J.; Angood, A. *Journal of Polymer Science Part A-2: Polymer Physics* **1970**, *8*, 1787–1796.

[113] Tasaki, K. *Journal of the American Chemical Society* **1996**, *118*, 8459–8469.

[114] Schild, H. *Progress in Polymer Science* **1992**, *17*, 163–249.

[115] Kubota, K.; Fujishige, S.; Ando, I. *Journal of Physical Chemistry* **1990**, *94*, 5154–5158.

[116] Kubota, K.; Fujishige, S.; Ando, I. *Polymer Journal* **1990**, *22*, 15–20.

[117] Okahata, Y.; Noguchi, H.; Seki, T. *Macromolecules* **1986**, *19*, 493–494.

[118] Okano, T.; Bae, Y.; Jacobs, H.; Kim, S. *Journal of Controlled Release* **1990**, *11*, 255–265.

[119] Hoffman, A.; Afrassiabi, A.; Dong, L. *Journal of Controlled Release* **1986**, *4*, 213–222.

[120] Hoffman, A. *Journal of Controlled Release* **1987**, *6*, 297–305.

[121] Li, P.-F.; Ju, X.-J.; Chu, L.-Y.; Xie, R. *Chemical Engineering & Technology* **2006**, *29*, 1333–1339.

[122] Iwata, H.; Oodate, M.; Uyama, Y.; Amemiya, H.; Ikada, Y. *Journal of Membrane Science* **1991**, *55*, 119–130.

[123] Peppas, N.; Khare, A. *Advanced Drug Delivery Reviews* **1993**, *11*, 1–35.

[124] O'Haver, T. *Peak Fitter*, Version 5.5. http://terpconnect.umd.edu/~toh/spectrum/InteractivePeakFitter.htm, 2014.

[125] Chu, L.-Y.; Niitsuma, T.; Yamaguchi, T.; Nakao, S.-I. *American Institute of Chemical Engineers Journal* **2003**, *49*, 896–909.

[126] Schild, H.; Tirrell, D. *Journal of Polymer Chemistry* **1990**, *94*, 4352–4356.

[127] Yang, Y.; Zeng, F.; Tong, Z.; Liu, X.; Wu, S. *Journal of Polymer Science B: Polymer Physics* **2001**, *39*, 901–907.

[128] Prevot, M.; Dejugnat, C.; Mohwald, H.; Sukhorukov, G. *ChemPhysChem* **2006**, *7*, 2497–2502.

[129] Park, T.; Hoffman, A. *Macromolecules* **1993**, *26*, 5045–5048.

[130] Deng, Y.; Li, Y.; Dai, J.; Lang, M.; Huang, X. *Journal of Polymer Science A: Polymer Chemistry* **2011**, *49*, 1582–1590.

[131] Kong, H.; Li, W.; Gao, C.; Yan, D.; Jin, Y.; Walton, D.; Kroto, H. *Macromolecules* **2004**, *37*, 6683–6686.

[132] Bittrich, E.; Burkert, S.; Muller, M.; Eichhorn, K.-J.; Stamm, M.; Uhlmann, P. *Langmuir* **2012**, *28*, 3439–3448.

[133] Zhu, X.; Yan, C.; Winnik, F.; Leckband, D. *Langmuir* **2007**, *23*, 162–169.

[134] Ishida, N.; Biggs, S. *Macromolecules* **2010**, *43*, 7269–7276.

[135] Plunkett, K.; Zhu, X.; Moore, J.; Leckband, D. *Langmuir* **2006**, *23*, 4259–4266.

[136] Liu, R.; Arabale, G.; Kim, J.; Sun, K.; Lee, Y.; Ryu, C.; Lee, C. *Carbon* **2014**, *77*, 933–938.

[137] Torrey, H. *Physical Review* **1956**, *104*, 563–565.

[138] Stejskal, E.; Tanner, J. *The Journal of Chemical Physics* **1965**, *42*, 288–292.

[139] Paudel, K.; Wu, J.; Hinds, B.; Stinchcomb, A. *Journal of Pharmaceutical Sciences* **2012**, *101*, 3823–2832.

[140] Kalyanasundaram, K. *Coordination Chemistry Reviews* **1982**, *46*, 159–244.

[141] Oesterhelt, F.; Rief, M.; Gaub, H. *New Journal of Physics* **1999**, *6*, 6.1–6.11.

[142] Bhat, R.; Timasheff, S. *Protein Science* **1992**, *1*, 1133–1143.

[143] Linegar, K.; Adeniran, A.; Kostko, A.; Anisimov, M. *Colloid Journal* **2010**, *72*, 279–281.

[144] Holyst, R.; Bielejewska, A.; Szymanski, J.; Wilk, A.; Patkowski, A.; Gapinski, J.; Zywocinshi, A.; Kalwarczyk, T.; Kalwarczyk, E.; Tabaka, M.; Ziebacz, N.; Wieczorek, S. *Physical Chemistry Chemical Physics* **2009**, *11*, 9025–9032.

[145] Zhang, W.; Zou, S.; Wang, C.; Zhang, X. *Journal of Physical Chemistry B* **2000**, *104*, 10258–10264.

[146] Kubota, K.; Hamano, K.; Kuwahara, N.; Fujishige, S.; Ando, I. *Polymer Journal* **1990**, *22*, 1051–1057.

[147] Ke, X.-X.; Wang, L.; Xu, J.-T.; Du, B.-Y.; Tu, Y.-F.; Fan, Z.-Q. *Soft Matter* **2014**, *10*, 5201–5211.